

Mapping dusty galaxy growth at $z > 5$ with FRESCO: Detection of $H\alpha$ in submm galaxy HDF850.1 and the surrounding overdense structures

Thomas Herard-Demanche^{1*}, Rychar J. Bouwens¹, Pascal A. Oesch^{2,3}, Rohan P. Naidu⁴, Roberto Decarli⁵, Erica J. Nelson⁶, Gabriel Brammer², Andrea Weibel³, Mengyuan Xiao³, Mauro Stefanon^{7,8}, Fabian Walter⁹, Jorryt Matthee¹⁰, Romain A. Meyer^{3,9}, Stijn Wuyts¹¹, Naveen Reddy¹², Pablo Arrabal Haro¹³, Helmut Dannerbauer^{14,15}, Alice E. Shapley¹⁶, John Chisholm¹⁷, Pieter van Dokkum¹⁸, Ivo Labbe¹⁹, Garth Illingworth²⁰, Daniel Schaerer³, Irene Shivaie²¹

¹Leiden Observatory, Leiden University, NL-2300 RA Leiden, Netherlands

²Cosmic Dawn Center (DAWN), Niels Bohr Institute, University of Copenhagen, Jagtvej 128, København N, DK-2200, Denmark

³Department of Astronomy, University of Geneva, Chemin Pegasi 51, 1290 Versoix, Switzerland

⁴MIT Kavli Institute for Astrophysics and Space Research, 77 Massachusetts Ave., Cambridge, MA 02139, USA

⁵INAF - Osservatorio di Astrofisica e Scienza dello Spazio di Bologna, Via Gobetti 93/3, 40129, Bologna, Italy

⁶Department for Astrophysical and Planetary Science, University of Colorado, Boulder, CO 80309, USA

⁷Departament d'Astronomia i Astrofisica, Universitat de València, C. Dr. Moliner 50, E-46100 Burjassot, València, Spain

⁸Unidad Asociada CSIC "Grupo de Astrofisica Extragaláctica y Cosmología" (Instituto de Física de Cantabria - Universitat de València)

⁹Max-Planck-Institut für Astronomie, Königstuhl 17, D-69117 Heidelberg, Germany

¹⁰Department of Physics, ETH Zürich, Wolfgang-Pauli-Strasse 27, Zürich, 8093, Switzerland

¹¹Department of Physics, University of Bath, Claverton Down, Bath, BA2 7AY, UK

¹²Department of Physics and Astronomy, University of California, Riverside, 900 University Avenue, Riverside, CA 92521, USA

¹³NSF's National Optical-Infrared Astronomy Research Laboratory, 950 N. Cherry Avenue, Tucson, AZ 85719, USA

¹⁴Instituto Astrofisica de Canarias (IAC), E-38205 La Laguna, Tenerife, Spain

¹⁵Universidad de La Laguna, Dpto. Astrofisica, E-38206 La Laguna, Tenerife, Spain

¹⁶Department of Physics & Astronomy, University of California, Los Angeles, 430 Portola Plaza, Los Angeles, CA 90095, USA

¹⁷Department of Astronomy, The University of Texas at Austin, 2515 Speedway, Stop C1400, Austin, TX 78712-1205, USA

¹⁸Astronomy Department, Yale University, 52 Hillhouse Ave, New Haven, CT 06511, USA

¹⁹Centre for Astrophysics and Supercomputing, Swinburne University of Technology, Melbourne, VIC 3122, Australia

²⁰Department of Astronomy and Astrophysics, University of California, Santa Cruz, CA 95064, USA

²¹Centro de Astrobiología (CAB), CSIC-INTA, Ctra. de Ajalvir km 4, Torrejón de Ardoz, E-28850, Madrid, Spain

Accepted XXX. Received YYY; in original form 2023 September 8

ABSTRACT

We report the detection of a 13σ $H\alpha$ emission line from HDF850.1 at $z = 5.188 \pm 0.001$ using the FRESCO NIRCcam F444W grism observations. Detection of $H\alpha$ in HDF850.1 is noteworthy, given its high far-IR luminosity, substantial dust obscuration, and the historical challenges in deriving its redshift. HDF850.1 shows a clear detection in the F444W imaging data, distributed between a northern and southern component, mirroring that seen in [CII] from the Plateau de Bure Interferometer. Modeling the SED of each component separately, we find that the northern component has a higher mass, star formation rate (SFR), and dust extinction than the southern component. The observed $H\alpha$ emission appears to arise entirely from the less-obscured southern component and shows a similar $\Delta v \sim +130$ km/s velocity offset to that seen for [CII] relative to the source systemic redshift. Leveraging $H\alpha$ -derived redshifts from FRESCO observations, we find that HDF850.1 is forming in one of the richest environments identified to date at $z > 5$, with 100 $z = 5.17$ – 5.20 galaxies distributed across 10 structures and a $\sim(15 \text{ cMpc})^3$ volume. Based on the evolution of analogous structures in cosmological simulations, the $z = 5.17$ – 5.20 structures seem likely to collapse into a single $>10^{14} M_\odot$ cluster by $z \sim 0$. Comparing galaxy properties forming within this overdensity with those outside, we find the masses, SFRs, and UV luminosities inside the overdensity to be clearly higher. The prominence of $H\alpha$ line emission from HDF850.1 and other known highly-obscured $z > 5$ galaxies illustrates the potential of NIRCcam-grism programs to map both the early build-up of IR-luminous galaxies and overdense structures.

Key words: galaxies: evolution – galaxies: high-redshift – large scale structures, protoclusters

1 INTRODUCTION

One of the most important frontiers in extragalactic astronomy has been understanding the formation and evolution of massive galaxies

* email: herard@strw.leidenuniv.nl

in the early universe. Despite the many significant insights that have been gained into both the build-up of the star formation rates (SFRs) and stellar masses of UV-bright galaxies from both space and ground-based telescopes (e.g., Madau & Dickinson 2014; Davidzon et al. 2017; Stefanon et al. 2021a; Bouwens et al. 2021; Harikane et al. 2022), it is essential we achieve an equally complete census of star formation from obscured galaxies given how significantly obscured star formation contributes to galaxies with masses $>10^{10} M_{\odot}$ (e.g. Reddy et al. 2006, 2008; Whitaker et al. 2017).

In addition to the great strides made by ALMA in this area (e.g., Casey et al. 2021; Smail et al. 2021; Bouwens et al. 2022; Dayal et al. 2022), a JWST is further revolutionizing this science area thanks to its sensitive near-IR photometric and spectroscopic capabilities to $5\mu\text{m}$ and beyond, sampling bright Balmer and Paschen series line like $H\alpha$, $Pa\alpha$, and $Pa\beta$ to $z \sim 7$ (e.g. Helton et al. 2023; Álvarez-Márquez et al. 2023a; Reddy et al. 2023). Through the identification of bright line emission from e.g. $H\alpha$ (e.g., the candidate $z = 5.58$ dusty galaxy shown in Oesch et al. 2023), one can assemble substantial spectroscopic samples of far-IR luminous, dusty star-forming galaxies in the early universe with JWST. Particularly useful for this endeavor are NIRCcam grism observations that allow for a probe of $H\alpha$ emission over the full morphology of sources over a ~ 9 arcmin² NIRCcam field, facilitating redshift determinations even when the escape of $H\alpha$ occurs over just an isolated region.

In this paper, we report on the successful detection of $H\alpha$ emission from HDF850.1, one of the first sub-millimeter galaxies to be identified in the high-redshift universe, leveraging new grism observations from the First Reionization Era Spectroscopically Complete Observations (FRESCO: Oesch et al. 2023) program. HDF850.1 was initially identified using sensitive sub-millimeter observations over the Hubble Deep Field (HDF) North with the SCUBA camera (Hughes et al. 1998), but no optical counterpart could be identified in the deepest HST images available at the time. Based on the available information, HDF 850.1 appeared to have a redshift $z > 2$, implying that the star formation rate of this single source could rival the total star formation activity of all coeval galaxies in the HDF combined. This discovery triggered a >10 -year effort to improve the location of the source from the coarse position provided by the $17''$ FWHM SCUBA beam, to search for possible counterparts, and to pin down its redshift (Richards 1999; Downes et al. 1999; Dunlop et al. 2004; Wagg et al. 2007; Cowie et al. 2009).

A redshift for HDF 850.1 was finally obtained through a millimeter line-scan obtained at the IRAM Plateau de Bure Interferometer (PdBI) by Walter et al. (2012) who detected multiple lines in the rest-frame sub-millimeter ([CII] as well as multiple CO lines), thus unambiguously pinpointing the redshift to $z = 5.183$. This study also revealed that the system is part of a fairly significant galaxy overdensity at these redshifts. Higher resolution imaging of the [CII] line emission from HDF 850.1 (Neri et al. 2014) provided evidence that HDF 850.1 is a merging system.

In addition to enabling the detection of the $H\alpha$ line from HDF850.1, the new NIRCcam imaging observations from FRESCO allow us to measure the continuum flux from HDF850.1 in the rest-optical while facilitating a modeling of the overall SED of both components of the source. Moreover, the NIRCcam grism observations allow for the identification of a large number of $H\alpha$ emitters over a ~ 62 arcmin² FRESCO area in the GOODS North field, allowing us to map out the $z = 5.17\text{--}5.20$ overdensity much more extensively than had been possible in earlier work by Walter et al. (2012), Arrabal Haro et al. (2018), and Calvi et al. (2021).

We organize the paper as follows. In §2, we provide a summary of the observational data we utilize for this analysis and describe

our procedures for constructing multi-wavelength catalogs. In §3, we describe our discovery of a detection of $H\alpha$ from HDF850.1, the photometry we derive for the two components of HDF850.1 and inferences based on SED modeling, and then present information on both the structure of the $z = 5.17\text{--}5.20$ overdensity in which HUDF850.1 resides, and on the characteristics of the large number of other member galaxies. In §4, we briefly discuss the potential of NIRCcam grism surveys for mapping out the build-up of massive galaxies in the early universe given the discovery of $H\alpha$ emission from HDF850.1 and a significant fraction of other well-known far-IR luminous $z > 5$ galaxies over the GOODS-North field. In §5, we include a short summary of our primary results and provide a brief look to the future. For consistency with previous work, we express all quantities using the so-called concordance cosmology with $\Omega_m = 0.3$ and $\Omega_{\Lambda} = 0.7$, $H_0 = 70$ km/s/Mpc. Stellar masses and SFRs are presented assuming a Chabrier (2003) IMF. All magnitudes are presented using the AB magnitude system (Oke & Gunn 1983).

2 DATA

2.1 FRESCO NIRCcam Grism and Imaging Data

In this analysis we make use of NIRCcam data obtained by the JWST FRESCO survey (GO-1895; see Oesch et al. 2023 for details). FRESCO covered both the GOODS-South and the GOODS-North fields with ~ 62 arcmin² of NIRCcam/grism spectroscopy in the F444W filter. This coverage is achieved with two 2×4 mosaics of NIRCcam/grism observations with significant column overlap in order to maximize the wavelength coverage over the field. Only the GRISMR was used due to overhead costs. The maximal wavelength coverage is from 3.8 to $5.0\mu\text{m}$, which is achieved over 73% of the full mosaic. The exposure times per pointing are 7043 s, resulting in an average 5σ line sensitivity of $\sim 2\times 10^{-18}$ erg s⁻¹ cm⁻² at a resolution of $R\sim 1600$. The grism data of GOODS-N used here were obtained in February 2023.

The NIRCcam/grism observations are reduced using the publicly available `grizli` code¹ (see also Brammer et al, in prep). Specifically, we start from the rate files that are obtained from the MAST archive. These are then aligned to a Gaia-matched reference frame. The direct images of a given visit are used to align the associated grism exposures. Before combination of the long-wavelength data, a custom bad-pixel map is applied, which masks residual bad pixels.

Following Kashino et al. (2022), we use a median filtering technique to remove the continuum spectra for each row of the individual grism exposures. The filter uses a 12 pixel central gap, which avoids self-subtraction in case of strong emission lines. After the first pass filtering, pixels with significant line flux are identified and masked, before running the median filtering again.

For each source of interest from the photometric catalog (see next section), we derive an extraction kernel based on the image morphology in the F444W band and the segmentation map. This kernel is used to perform an optimal extraction of 1D spectra from the aligned and combined grism exposures. We use slightly modified sensitivity curves and spectral traces based on the v4 grism configuration files².

In addition to the grism observations, FRESCO obtained imaging in the two short-wavelength filters F182M and F210M, as well as direct imaging in the long-wavelength filter F444W. The 5σ depths of

¹ <https://github.com/gbrammer/grizli>

² <https://github.com/npirzkal/GRISMCONF>

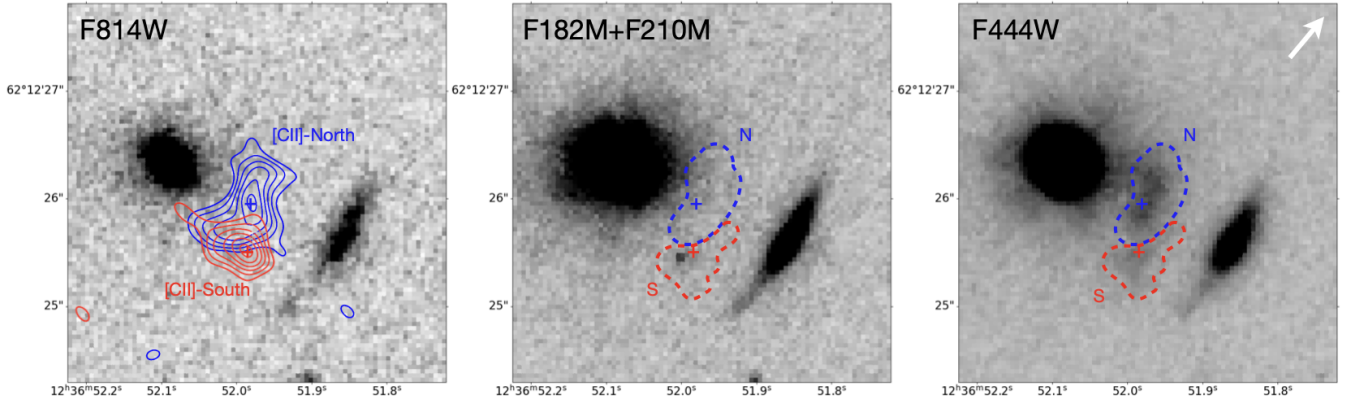


Figure 1. Images centered on HDF850.1 from both *HST* in the F814W band (*left panel*) and *JWST*/NIRCam in the F182M+F210M (*center panel*) and F444W bands (*right panel*). The blue and red solid lines contours in the left panel show the 3, 4, 5, 6, 7, and 8 σ contours for [CII] emission from the northern and southern components, respectively, of HDF850.1 as derived by [Neri et al. \(2014\)](#) using PdBI. Crosses give the spatial position where the [CII] emission for each component reaches a peak. The dashed contours shown in the center and right panels delineate the regions used in our extractions of near-IR spectra for the northern (*blue*) and southern (*red*) components. These two regions have been designed to mirror the shape and morphology of the two components in the F444W imaging data. The white arrow in the upper-right corner of the right panel shows the dispersion direction of the NIRCam grism.

these images are respectively 28.3, 28.1, and 28.2 mag, as measured in circular apertures of 0'32 diameter.

We note that deeper NIRCam imaging data are available over ~50% of the FRESCO mosaics thanks to observations from the JADES team ([Robertson 2022](#)). However, these data are not yet publicly available for inclusion in this analysis.

2.2 FRESCO Multi-Wavelength Catalogs

In addition to the new JWST NIRCam data, we also make use of all ancillary HST imaging available in the GOODS-North field. Being a key extragalactic field for more than a decade, GOODS North has been targeted by all the main telescope facilities through a large number of programs. A complete listing of HST programs can be found on the Hubble Legacy Field (HLF) release page³ (see also [Whitaker et al. 2019](#) and [Illingworth et al. 2016](#)). Most importantly, the field was covered with ACS imaging from GOODS ([Giavalisco et al. 2004](#)), with ACS and WFC3/IR imaging by the CANDELS survey ([Koekemoer et al. 2011](#); [Grogin et al. 2011](#)), as well as WFC3/IR grism imaging by the AGHAST survey ([Weiner & AGHAST Team 2014](#)).

Here, we use a re-reduction of all available HST ACS and WFC3/IR data in the archive in filters that cover the FRESCO pointings, which we drizzled to a common pixel frame of 40 mas/pixel as the JWST NIRCam data. The 5 σ depth (in the same 0'32 diameter apertures) for the ancillary data are well-matched to the FRESCO NIRCam imaging: they range from ~28.6 mag for the ACS data (F435W, F606W, F775W, F814W, and F850LP) to ~28.2 mag for the WFC3/IR data (F105W, F125W, F160W), with the exception of F140W that reaches to ~27.4 mag.

In total, we derive photometry in 12 bands for the GOODS-North data set. The F444W images are used as a detection image, and we run SExtractor ([Bertin & Arnouts 1996](#)) in dual image mode to measure matched-aperture photometry. The images are all PSF-matched to the F444W detection image, and fluxes are corrected to total using the default SExtractor AUTO parameters in addition to a

small correction for remaining flux outside the AUTO aperture based on WebbPSF's F444W curve of growth ([Perrin et al. 2014](#)).

2.3 Spectroscopic Sample of $H\alpha$ Emitters

We briefly summarize the construction of the $H\alpha$ catalog at $z \approx 4.9 - 6.6$ over the GOODS-North FRESCO field and refer readers to [Brammer et al. \(2023, in prep\)](#) and [Naidu et al. \(2023, in prep\)](#) for more detailed description of the overall methods and catalog validation. Line extractions from the grism data are based on EAZY photometric redshifts (z_{phot}). For each object, we search for lines in a window around $z_{\text{phot}} \pm 0.05 \times (1 + z_{\text{phot}})$. The photometric redshifts are derived from the PSF-matched photometry described above (§2.2). Additionally, we also use the default *grizli* photometric redshifts catalog that uses a stack of the FRESCO imaging (F182M+F210M+F444W) as a detection image, and makes two different choices in performing the photometry (e.g., with different source deblending parameters). We use both sets of photometric redshifts to marginalize over such choices. In practice, the best-fit redshifts at $z_{\text{phot}} > 4.5$ have a small median difference of $|\Delta_z| < 0.1$ and in most cases result in the same line-candidates, but a fraction ($\approx 25\%$) have $|\Delta_z| > 0.3$.

Every line extracted with $S/N > 5$ is visually inspected to verify that its morphology is consistent with the source and also to look for false positives (e.g., from broad PAH features in the foreground that slip through the median filtering). Physical properties (e.g., stellar masses) are derived by jointly fitting the photometry and line-fluxes with a non-parametric star-formation history and Chabrier IMF using the Prospector SED-fitting code ([Leja et al. 2017a](#)). We refer readers to [Naidu et al. \(2023, in prep\)](#) for further details about the modeling choices.

3 RESULTS

3.1 Identification of $H\alpha$ Emission from HDF850.1

One of the first sources we examined after creating catalogs of line emitting sources over the GOODS-North FRESCO field was the well-

³ <https://archive.stsci.edu/prepds/hlf/>

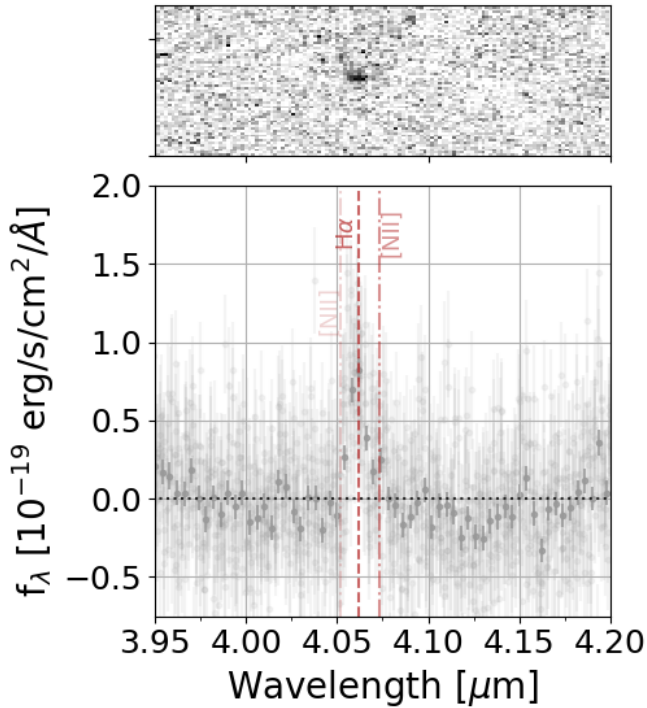


Figure 2. 2D spectrum from the southern component to HDF850.1 (*upper panel*) along with our 1D extraction from the direct image morphology (*lower panel*). The upper panel shows a zoomed-in 2D spectrum around the $H\alpha$ line after subtracting the continuum using a median-filtered technique following (Kashino et al. 2022; see §2.1). The black dashed lines in the lower panel show the positions of the $H\alpha$ line (13σ detection) and the $[\text{NII}]_{6585}$ line (4σ detection) at the fitted redshift of $z = 5.188$. The expected wavelength of the $[\text{NII}]_{6549}$ line ($\approx 3\times$ fainter than $[\text{NII}]_{6585}$; e.g. Dojčinović et al. 2023) is also shown but does not show a significant detection in the FRESCO data.

known dusty star-forming galaxy HDF850.1 with a spectroscopic redshift $z = 5.1853$ from the $157.74\mu\text{m}$ $[\text{CII}]$ line (Walter et al. 2012; Neri et al. 2014). As we discussed in §1, that source evaded a direct redshift determination for >10 years following its initial discovery (e.g. Wagg et al. 2007), and a redshift only came in 2012 thanks to a dedicated spectral scan for $[\text{CII}]$ and various CO lines with PdBI (Walter et al. 2012).

The *JWST* F182M, F210M, and F444W NIRC*am* imaging we have available for HDF850.1 from FRESCO is shown in the center and right panels of Figure 1 together with the blueshifted and redshifted high spatial resolution $[\text{CII}]$ contours from PdBI. Also shown is the imaging data of HDF850.1 at $0.8\mu\text{m}$ from F814W, again demonstrating that HDF850.1 radiates essentially no flux at $<1\mu\text{m}$. From this imaging data, it is clear that while both components are detected in the NIRC*am* F444W data, only the southern component shows a clear detection in the F182M and F210M imaging data.

We made use of the two prominent components of HDF850.1 in the F444W imaging data to construct segmentation maps, shown in the central and right panels of Figure 1 as red and blue dashed lines. We then used *grizli* to extract spectra of each component. In Figure 2, we show both a two-dimensional and one-dimensional spectral extraction for the southern component to HDF850.1. In the lower panel to Figure 2, we present a collapsed one-dimensional spectrum which not only reveals a 13σ detection of the $H\alpha$ line, but shows the detection of $[\text{NII}]_{6583}$ at 4σ from HDF850.1. No significant detection of $[\text{NII}]_{6548}$ is apparent in the FRESCO grism

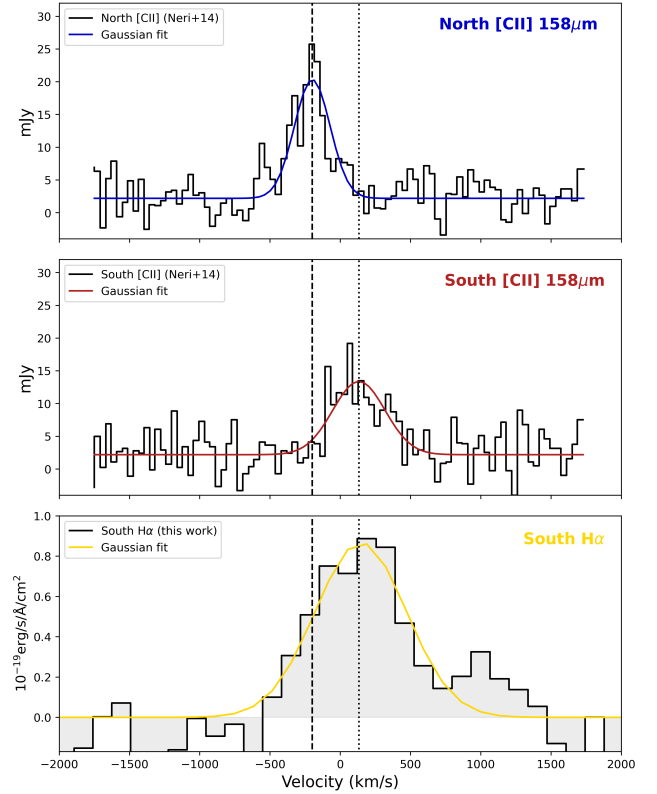


Figure 3. Comparison between the $[\text{CII}]$ detection from Neri et al. (2014) and our $H\alpha$ detection for both components. The upper two rows show the $[\text{CII}] P_{3/2} \rightarrow P_{1/2}$ line above the dust continuum from both component of HDF850.1 (*black lines*) as well as the Gaussian fit to the lines (*blue and red lines*) derived by Neri et al. (2014). The lowest row shows our detected $H\alpha$ line (*black*) along with a Gaussian fit for the southern component (*yellow*). Velocities for the $[\text{CII}]_{158\mu\text{m}}$ and $H\alpha$ lines are shown relative to the $[\text{CII}]_{158\mu\text{m}}$ redshift determined by Neri et al. (2014) of $z = 5.1853$ (307.267 GHz). The dashed and dotted vertical lines are shown at the centroids of the Gaussian fits to $[\text{CII}]$ for the northern and southern components of HDF850.1, respectively, to highlight the coinciding feature in the southern component.

spectra, but this is not surprising given the fact that $[\text{NII}]_{6548}$ is $\approx 3\times$ fainter than $[\text{NII}]_{6583}$ (e.g. Dojčinović et al. 2023).

For $H\alpha$, we measure a total flux of $(6.4 \pm 0.5) \times 10^{-18}$ erg/s/cm² for the southern component to HDF850.1 and derive a redshift of 5.188 ± 0.001 . The $[\text{NII}]/H\alpha$ ratio we measure for the Southern component to HDF850.1 is 0.4 ± 0.1 . Such a high $[\text{NII}]/H\alpha$ ratio is commonly found for galaxies at higher masses with solar metallicities (e.g. Shapley et al. 2015). Shocks could also be a contributing factor to the high $[\text{NII}]/H\alpha$ ratio we find (e.g. Kewley et al. 2013; Freeman et al. 2019) – which would not be especially surprising given the apparent merging activity in HDF850.1 based on its two component structure (Neri et al. 2014).

The redshift measurement we derived from the $H\alpha$ line implies a velocity offset of 133 ± 34 km/s relative the systemic redshift measurement $z = 5.1853$ derived by Neri et al. (2014). Neri et al. (2014) find a velocity offset of 130 km/s for the $[\text{CII}]$ line from the southern component to HDF850.1, which is almost exactly the same velocity offset in $[\text{CII}]$ for the southern component as we find here. A detailed comparison of the line profiles and intensity of our new $H\alpha$ detection is shown in Figure 3 for the Southern component to HDF850.1, both in terms of the raw extraction (*gray histogram*) and Gaussian fits to

the lines (*yellow lines*). Figure 3 also shows the line profiles for the northern and southern components to HDF850.1 as found by Neri et al. (2014). To further emphasize this similarity, a vertical dotted line is shown at the velocity offset for the southern component found by Neri et al. (2014). From Figure 4, it is furthermore clear that $H\alpha$ emission we detect (*white contours*) appears to mostly originate from the southern component of HDF850.1, being offset from both the [CII] and continuum IR emission lying to the north (*blue and orange contours, respectively*).

Additionally, the $H\alpha$ line we extract from the southern component of HDF850.1 appears to be very broad overall. Ignoring for the moment the impact spatial extension has on the width of the lines, the best-fit FWHM we find for the Southern component is of 7.6×10^2 km/s. To account for the impact that source morphology has in broadening the line, we make use of *grizli* to forward model the source based on its direct image morphology using the same dispersion direction as in the observations. Based on this forward modeling, we find that the non-zero size of HDF850.1 contributes 6.2×10^2 km/s to the measured FWHMs. Subtracting this contribution in quadrature from the southern component, we derive a FWHM of $(4.4 \pm 0.9) \times 10^2$ km/s. The width of this line is therefore consistent with what Neri et al. (2014) derive for [CII] from the southern component. Given similar velocity offsets for both lines (130 km/s for [CII] vs. $(1.3 \pm 0.3) \times 10^2$ km/s for $H\alpha$), it seems clear that ISM material producing both lines show a very similar kinematic structure.

In contrast to the southern component, the northern component of HDF850.1 does not show a clear, localized detection of $H\alpha$ line emission. As a result and due to the proximity of the two components and dispersion direction (shown in Figure 1), line emission from the southern component partially extends into the same spatial region where $H\alpha$ line flux measurements need to be made for the northern component. As a result of these challenges, we only report an upper limit to the $H\alpha$ flux for the northern component of $f_{H\alpha} < 2.1 \times 10^{-18}$ erg/s/cm² (3σ). We derived this upper limit by comparing the observations with the spatial profile expected for $H\alpha$ emission from the northern component assuming a similar spatial distribution to the continuum light in the direct image. By computing the 2D least squares residuals between the expected and observed line morphologies, we concluded that there is no significant $H\alpha$ line flux emanating from the northern component, and any line flux evident in the segmentation map for the northern component is consistent with contamination from the southern component. The flux measurements for the two components are provided in Table 1.

3.2 Impact of Dust Obscuration on the $H\alpha$ Line Emission

Thanks to our new measurements of the $H\alpha$ fluxes for both components of HDF850.1, we can compute an observed SFR for each component. By comparing this SFR to the SFR implied by the respective [CII] luminosities, we can attempt to estimate the approximate dust obscuration of each component. We use the conversion factor from Kennicutt & Evans (2012):⁴

$$SFR_{H\alpha} = L_{H\alpha} (M_{\odot}/yr) / (10^{41.27} \text{ erg/s}) \quad (1)$$

The SFR we estimate from the observed $H\alpha$ flux for the southern component is $6.0 \pm 0.5 (1.5/\mu) M_{\odot}/yr$, while for the northern component the SFR we estimate is $< 1.8 (1.7/\mu) M_{\odot}/yr$. In specifying

⁴ While we present SFRs and stellar masses using the Chabrier (2003) IMF and Kennicutt & Evans (2012) presents their SFR relations using Kroupa & Weidner (2003) IMF, Kennicutt & Evans (2012) emphasize that the relation for a Chabrier (2003) IMF is virtually identical.

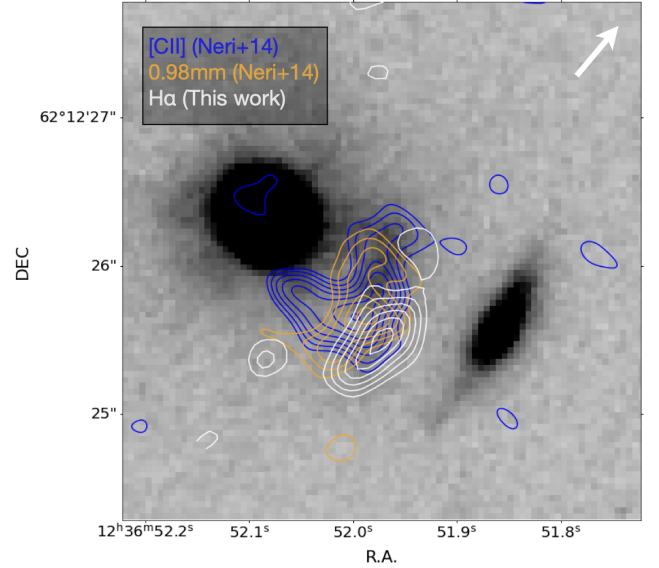


Figure 4. Spatial distribution of line and dust emission relative to the JWST NIRCam F444W imaging observations of HDF850.1. The extracted $H\alpha$ map is shown in white contours over the JWST NIRCam F444W imaging. The velocity averaged [CII]_{158 μ m} line detection and the 0.98mm dust continuum from Neri et al. (2014) are shown for comparison. All contours start at 3σ and increase in steps of 1σ .

the SFR for each source, we have divided the result by the fiducial magnification factors for the two components derived in Neri et al. (2014) based on the isothermal model they constructed for a nearby $z = 1.224$ elliptical galaxy, i.e., 1.7 for the northern component and 1.5 for the southern component. Our quoted results in Table 1 include the factors $(1.7/\mu)$ and $(1.5/\mu)$ for clarity and to allow for a scaling of the results in case of updated lensing magnification factors.

We can estimate the approximate dust extinction for each component by relying on the measured [CII] luminosities for HDF850.1 from Neri et al. (2014) to estimate the total SFRs. The ALPINE program (Le Fèvre et al. 2020; Béthermin et al. 2020; Faisst et al. 2020) provided the following calibration of the $L_{[CII]}$ -SFR relation (Schaerer et al. 2020):

$$SFR_{[CII]} = (L_{[CII]} / 10^{6.61} L_{\odot})^{0.855} (M_{\odot}/yr) \quad (2)$$

We infer [CII] SFRs of $(1.6 \pm 0.5) \times 10^2 (1.7/\mu) M_{\odot}/yr$ and $(0.9 \pm 0.3) \times 10^2 (1.5/\mu) M_{\odot}/yr$ for the northern and southern components to HDF850.1.

Dividing the apparent $H\alpha$ SFRs by the [CII] SFRs, we infer $SFR_{H\alpha}/SFR_{[CII]}$ ratios of < 0.01 and 0.07 ± 0.03 , respectively, demonstrating that even in the case of the clear detection of $H\alpha$ from the southern component of HDF850.1, dust attenuation would nevertheless appear to have a substantial impact on the observed line emission. The $SFR_{H\alpha}/SFR_{[CII]}$'s we infer here are similar to what would be suggested by the A_V 's we derive for the two components in §3.3.2, i.e., $\sim 0.02^{+0.04}_{-0.01}$ and $\sim 0.12^{+0.25}_{-0.10}$.

3.3 UV+Optical+far-IR SED Model of HDF850.1

3.3.1 Photometry on the Individual Components of HDF850.1

Because of the very extended wings to the profile from a bright nearby elliptical galaxy, obtaining accurate flux measurements for

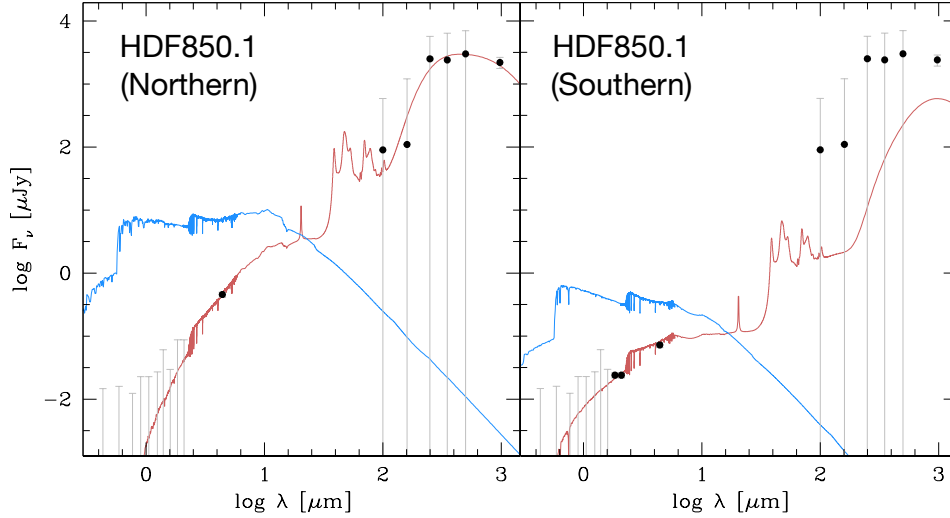


Figure 5. Model spectral energy distribution derived by MAGPHYS to the northern and southern components of HDF850.1. Blue and red lines show the emission from stars and from dust, respectively. Optical and near-IR photometry shown with the solid circles (and 1σ uncertainties) for both components are from Table 2 and the far-IR constraints from Herschel as presented in [Walter et al. \(2012\)](#) and dust continuum at 0.9 mm from [Neri et al. \(2014\)](#). Since the spatial resolution of the Herschel observations ($>15''$) is insufficient to provide independent measurements of the flux of each component of HDF850.1, we assume that the relative flux in each component is 50%, similar to what is seen in the far-IR continuum from PdBI. The procedure for performing the SED fits is detailed in §3.3.2.

Table 1. Inferred characteristics of the two components of HDF850.1

Northern Component	
Lensing Magnification μ	1.7^a
$L_{[\text{CII}]}$	$1.6 \times 10^9 (1.7/\mu)^a L_\odot$
$\text{SFR}_{[\text{CII}]}$	$(1.6 \pm 0.5) \times 10^2 (1.7/\mu)^a M_\odot/\text{yr}$
$v_{[\text{CII}]}$	-200 km/s
$\text{FWHM}_{[\text{CII}]}$	300 km/s
$f_{\text{H}\alpha}$	$< 2.1 \times 10^{-18} \text{ erg/s/cm}^2 [3\sigma]$
$\text{SFR}_{\text{H}\alpha}$	$< 1.8 (1.7/\mu) M_\odot/\text{yr}$
$\text{SFR}_{\text{H}\alpha} / \text{SFR}_{[\text{CII}]}$	< 0.01
τ_V	$3.9^{+0.6}_-0.8^b$
$\log_{10} M^*/M_\odot$	$10.3^{+0.3}_{-0.3} + \log_{10}(1.7/\mu)^b$
$\log_{10} L_{\text{IR}}$	$11.9^{+0.1}_{-0.2} + \log_{10}(1.7/\mu)^b$
$\text{SFR}_{\text{MAGPHYS}}$	$64^{+38}_{-17} (1.7/\mu)^b M_\odot/\text{yr}$
Southern Component	
Lensing Magnification μ	1.5^a
$L_{[\text{CII}]}$	$0.8 \times 10^9 (1.5/\mu)^a L_\odot$
$\text{SFR}_{[\text{CII}]}$	$(0.9 \pm 0.3) \times 10^2 (1.5/\mu)^a M_\odot/\text{yr}$
$v_{[\text{CII}]}$	130^a km/s
$\text{FWHM}_{[\text{CII}]}$	410 km/s
$f_{\text{H}\alpha}$	$(6.5 \pm 0.4) \times 10^{-18} \text{ erg/s/cm}^2$
$v_{\text{H}\alpha}$	$(1.3 \pm 0.3) \times 10^2 \text{ km/s}$
$\text{FWHM}_{\text{H}\alpha + [\text{NII}]}$	$(4.4 \pm 0.9) \times 10^2 \text{ km/s}$
$\text{SFR}_{\text{H}\alpha}$	$(6.5 \pm 0.5) (1.5/\mu) M_\odot/\text{yr}$
$\text{SFR}_{\text{H}\alpha} / \text{SFR}_{[\text{CII}]}$	0.07 ± 0.03
τ_V	$2.1^{+1.6}_{-1.1}^b$
$\log_{10} M^*/M_\odot$	$8.9^{+0.1}_{-0.1} + \log_{10}(1.5/\mu)^b$
$\log_{10} L_{\text{IR}}$	$10.3^{+0.4}_{-0.3} + \log_{10}(1.5/\mu)^b$
$\text{SFR}_{\text{MAGPHYS}}$	$2.1^{+3.3}_{-0.8} (1.5/\mu)^b M_\odot/\text{yr}$

^a From [Neri et al. \(2014\)](#)

^b Derived using MAGPHYS (§3.3.2: see Figure 5)

Table 2. Photometry Derived for HDF850.1

Band	Flux [AB mag] ^{a,b}
Northern Component	
F435W	>29.0
F606W	>28.9
F775W	>29.2
F850LP	>28.5
F105W	>28.5
F125W	>28.3
F140W	>27.4
F160W	>28.2
F182M	>27.0
F210M	>27.0
F444W	24.0 ± 0.1
Southern Component	
F435W	>29.0
F606W	>28.9
F775W	>29.2
F850LP	>28.5
F105W	>28.5
F125W	>28.3
F140W	>27.4
F160W	>28.2
F182M	27.2 ± 0.1
F210M	27.2 ± 0.1
F444W	26.0 ± 0.1

^a Derived using GALFIT ([Peng et al. 2002: §3.3.1](#))

^b Upper limits are 2σ

HDF850.1 can be challenging to obtain using simple aperture photometry and therefore we elected to measure the flux for HUDF850.1 by modeling the light with analytic Sersic profiles using GALFIT ([Peng et al. 2002](#)). This provides a very effective way of coping with con-

tamination from the bright elliptical spilling over onto our aperture measurements.

We begin by using *galfit* to model the light in the NIRC*am* F444W band where both the northern and southern components of HDF850.1 are clearly detected, while also fitting to light in the nearby elliptical galaxy. We model the light in the southern component of HDF850.1 with a single Sersic profile and light from the northern component as the sum of three different Sersic profiles. After using these fits to measure the flux of both components to HDF850.1 in the F444W band, we fix the centers and shapes of the different contributors to both components and then refit the amplitudes in each passband.

To account for the uncertainties associated with the extended wings of the nearby elliptical galaxy, we alternatively make use of two different Sersic parameters $n = 2$ and $n = 5$ in fitting for the contribution from that galaxy. We take the flux uncertainty to be equal to the differences between the flux measurements in the two fits, and in cases where there is more than 0.4 mag differences between the flux measurements, we treat a component as undetected in a given passband.

We present the flux measurements we obtained for the two components of HDF850.1 in Table 2. We measure a F444W-band magnitude of 24.0 ± 0.1 mag for the northern component to HDF850.1 and 26.0 ± 0.2 mag for the southern component. We remark that the F444W flux we measure for the southern component is $\sim 4\times$ what we would expect accounting for the line emission from $H\alpha$ alone, suggesting that stellar continuum from HDF850.1 contributes substantially to the F444W flux that we measure for the southern component. For the northern component, the contribution from the stellar continuum seems to dominate the F444W flux given the absence of a clear line detection at its location.

3.3.2 SED Modeling of UV+Optical and far-IR Light from HDF850.1

The JWST NIRC*am* observations presented here provide us with the first direct constraints on the stellar content of HDF850.1. We complement the photometry listed in Table 2 with the flux limits in the Herschel bands reported in Walter et al. (2012), and the 1 mm flux density continuum reported for the two components of the system in Neri et al. (2014). We model the Spectral Energy Distribution of the northern and southern components of HDF 850.1 using the high-redshift implementation of MAGPHYS (da Cunha et al. 2008, 2015). MAGPHYS assumes energy balance between energy absorbed by dust in the rest-frame optical range and re-emitted in the far-infrared. The stellar population is modeled based on Bruzual & Charlot (2003)’s spectral libraries, and assuming a delayed exponential function as star formation history. The best-fit model is shown in Fig. 5. We infer the best fit of the free parameters and their uncertainties from the distribution of the posterior probabilities, interpolated at the 16%, 50% and 84% levels. Our best-fit stellar masses, star formation rates, far-IR luminosities, and dust attenuation for the two components of HDF850.1 are provided in Table 1.

The NIRC*am* observations sample the stellar continuum around the Balmer break, which lies at $2.1\mu\text{m}$. Our MAGPHYS fits suggest that both components of HDF850.1 are significantly dust reddened. The northern component of HDF850.1 appears more massive and star forming, albeit with a similar specific SFR, compared to the southern component. The precise flux measurements made possible thanks to our new NIRC*am* photometry pins down the stellar component of the fit; this however, combined with the energy balance assumption in the code, and the large uncertainties associated with the Herschel photometry of HDF850.1 as a whole, leads to the dust continuum

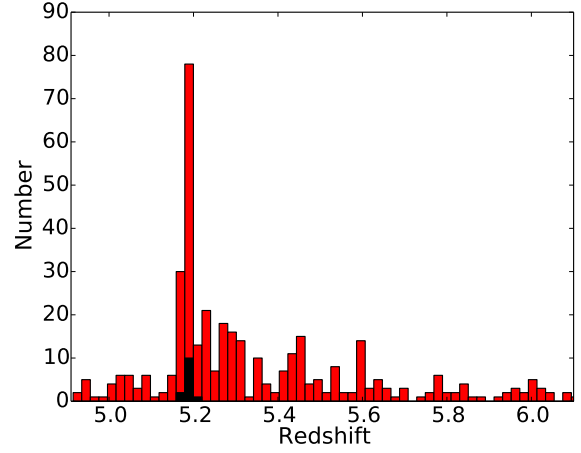


Figure 6. Redshift Distribution of Star-Forming Galaxies over the GOODS-North FRES*CO* field detected in $H\alpha$ at $>5\sigma$ (red histogram). Sources shown in black in the histogram were identified earlier as part of the spectroscopic sample of Walter et al. (2012) and Calvi et al. (2021). Clearly, there is strong evidence for a substantial spike in the redshift distribution of galaxies at $z = 5.17\text{-}5.20$, centered on the redshift of HUDF850.1. Twenty four of the sources in this redshift spike were identified earlier as part of the Arrabal Haro et al. (2018) analysis leveraging the SHARDS data set.

emission in the southern component of HDF850.1 being underestimated. A better sampling of the IR continuum emission separately for the two components of HDF850.1 is necessary to improve our characterization of the overall SED.

3.4 Extended Galaxy Structures Surrounding HDF850.1

3.4.1 Redshift Overdensity at $z \sim 5.2$ and Comparison with Earlier Studies

Given the substantial clustering of other star-forming galaxies expected around massive galaxies like HDF850.1 and earlier results showing a significant overdensity of galaxies at $z \sim 5.2$ (Walter et al. 2012; Arrabal Haro et al. 2018; Calvi et al. 2021), it is logical to make use of the substantial number of sources with spectroscopic redshifts in the GOODS North field from FRES*CO* to investigate this matter more extensively.

Using the techniques described in §2.3, we constructed catalogs of $H\alpha$ emitters over GOODS North FRES*CO* field. Figure 6 shows the number of sources as a function of redshift, and it is clear there is a huge overdensity of sources at $z = 5.17\text{-}5.20$, with 100 sources found in that narrow redshift interval. Walter et al. (2012) and Calvi et al. (2021) had both previously reported the same overdensity of galaxies at $z \sim 5.2$, adding 13 and 6 spectroscopic members, respectively. Analysis of the narrow-band SHARDS observations indicate 44 additional sources whose redshifts are consistent with lying in this overdensity (Arrabal Haro et al. 2018), but the redshift measurements from SHARDS are much less precise, i.e., $\Delta z \sim 0.07$, and so much more difficult to tie to distinct individual structures identified here.

Nineteen of the 100 $H\alpha$ emitters that we identified in the redshift range $z = 5.16$ to $z = 5.20$ were previously flagged as probable members of the $z \sim 5.2$ overdensity by Walter et al. (2012), Arrabal Haro et al. (2018), and Calvi et al. (2021). These earlier studies appear to have been most efficient at identifying those member galaxies in the $z \sim 5.2$ overdensity with the highest $H\alpha$ fluxes, likely as a result of

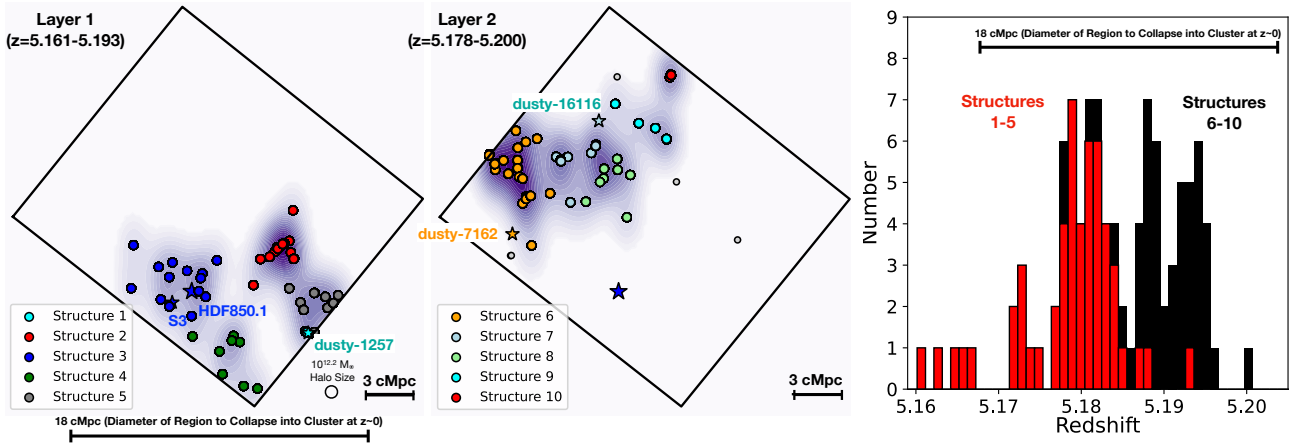


Figure 7. Spatial distribution of $H\alpha$ emitters (*left and center panels*) in the prominent overdensity at $z = 5.17$ - 5.20 in the GOODS-North FRESKO Field. The black lines enclose the area covered by the FRESKO F444W grism observations. Sources are shown in various color filled circles depending on the extended structure each was tentatively identified to belong based on the redshift and spatial position on the sky. Extended structures 1, 2, 3, 4, and 5 are presented in the left panel, while structures 6, 7, 8, 9, and 10 are presented in the center panel. The larger and smaller blue star show the position of HDF850.1 and another dusty star-forming galaxy S3 (see Figure 9) which appears to be part of the same extended structure 3. The orange, light blue, and cyan stars in the center panel show the positions of three dusty galaxies dusty-1257, dusty-7162, and dusty-16116 identified in extended structures 1, 6, and 7 by Xiao et al. (2023). The horizontal bars towards the lower region of the left and center panels indicate the comoving radii (3 cMpc) of the most extended structures identified here and the comoving diameter (18 cMpc; Chiang et al. 2017) of the regions of the universe at $z \sim 5.2$ that collapses into $>10^{14} M_{\odot}$ galaxy clusters by $z \sim 0$, respectively. The small open circle indicates the expected size of $10^{12.2} M_{\odot}$ halos at $z \sim 5.2$. The rightmost panel shows the number of sources as a function of redshift. Sources in extended structures 1-5, shown as the red histogram, are distributed more towards the southern and western parts of the FRESKO GOODS-North field and mostly have redshifts between 5.165 and 5.185. Meanwhile, sources in structures 6-10, shown as the black histogram, are distributed more towards the eastern and northern parts of the FRESKO field and mostly have redshifts between 5.185 and 5.196. The horizontal bar shows the comoving length scale (Chiang et al. 2017) of structures that collapse into $>10^{14} M_{\odot}$ galaxy cluster by $z \sim 0$. The Chiang et al. (2017) suggest that all 10 extended structures identified here likely collapse into a single $>10^{14} M_{\odot}$ galaxy cluster by $z \sim 0$.

Table 3. Extended structures Identified From $z = 5.16$ to $z = 5.31$ in the FRESKO GOODS North field^a

ID	RA	Structure Center		$\Delta\delta$ [cMpc]	z_{mean}	σ_v [km/s]	Radius [cMpc] ^b	δ_g ^c	$\log_{10} \Sigma_i$	# of Members	Noteworthy Members
		Dec	$\Delta\alpha$ [cMpc]						$M_{\text{halo},i}/M_{\odot}$ ^d		
1	12:36:25.01	62:11:18.4	8.1	-6.8	5.164	121	0.21	—	11.6	3	Dusty-1257
2	12:36:31.46	62:13:35.3	6.3	-1.6	5.178	164	0.79	267	11.8	14	
3	12:36:55.00	62:12:39.7	-0.0	-3.7	5.180	176	2.83	30	12.6	16	HDF850.1, S3
4	12:36:42.98	62:10:37.4	3.2	-8.4	5.180	112	2.39	30	11.8	8	
5	12:36:23.06	62:12:06.9	8.6	-5.0	5.184	211	0.74	33	11.5	9	Dusty-7162
6	12:37:15.51	62:15:34.5	-5.8	3.2	5.189	168	2.00	28	12.2	21	Dusty-26715
7	12:37:01.42	62:16:20.0	-1.8	4.7	5.194	54	0.95	80	11.2	8	
8	12:36:53.85	62:15:27.8	0.3	2.7	5.187	200	2.12	21	11.6	8	
9	12:36:44.98	62:16:58.4	2.7	6.2	5.190	163	0.43	127	11.4	5	
10	12:36:39.79	62:18:22.9	4.1	9.5	5.194	60	0.12	—	11.4	3	
11	12:37:03.90	62:12:26.5	-2.4	-4.2	5.220	182	2.23	21	12.1	9	Dusty-4014
12	12:37:21.89	62:14:38.2	-7.3	0.9	5.223	71	1.18	119	10.7	5	
13	12:36:34.76	62:16:56.2	5.5	6.3	5.268	275	1.49	12	11.1	5	
14	12:36:31.28	62:14:35.9	6.5	0.8	5.269	236	0.75	89	11.4	12	
15	12:36:26.99	62:14:24.3	7.7	0.4	5.301	165	0.66	54	12.5	8	GN10
16	12:36:30.00	62:17:33.8	6.8	7.8	5.301	67	0.86	—	10.6	3	
17	12:37:19.53	62:15:38.7	-6.8	3.3	5.302	211	2.09	8	11.6	4	
18	12:36:38.67	62:09:45.6	4.5	-10.5	5.308	216	1.79	—	10.8	3	

^a These structures are presented in Figures 7 and A1. See §3.4.2

^b Estimated using Eq. (3). Since the expected sizes of collapsed halos with masses of $10^{12.0}$ and $10^{12.2} M_{\odot}$ are 0.3 cMpc and 0.4 cMpc, respectively, this suggests that the identified overdensities are composed of extended structure, rather than represent galaxies within a single halo.

^c This is the estimated amplitude of the overdensity of $H\alpha$ emitters in the cylindrical volume enclosed within the estimated radius of the structure and a $|\Delta z| < 2\sigma_v/c$ relative to $H\alpha$ emitters over the entire FRESKO GOODS-North volume.

^d Four halos with mass $10^{12.0} M_{\odot}$ and one halo mass with mass $10^{12.2} M_{\odot}$ are expected within the FRESKO GOODS North $z = 5.0$ - 6.0 volume.

these same sources showing more prominent Ly α emission lines for redshift determinations. Three out of the seven brightest H α emitters (i.e., 43%) were identified as part of earlier spectroscopic studies, as well as five out of the 14 brightest H α emitters (i.e., 36%). This compares with just 19 out of 100 sources (i.e. 19%) that appeared in these earlier compilations.

Comparing our redshift measurements to those from [Walter et al. \(2012\)](#) and [Calvi et al. \(2021\)](#), the redshift measurements we derive are $\Delta z = -0.009 \pm 0.011$ lower in the mean than those in the literature. This is consistent with what we would expect for Ly α velocity offsets of 436 ± 582 km/s, in the general range of what has been found in many studies at $z \sim 3-8$ (e.g., [Erb et al. 2014](#); [Tang et al. 2023](#)). Somewhat unexpectedly, only six of the nineteen sources in the spectroscopic redshift catalogs of [Walter et al. \(2012\)](#) and [Calvi et al. \(2021\)](#) with coverage from FRESCO show up in our own catalogs of H α emitters. Given the high completeness levels expected for our H α -emitter searches, this suggests that previous spectroscopic samples were dominated by sources with high Ly α escape fractions.

There are three sources over the GOODS North field discussed by [Walter et al. \(2012\)](#) and [Calvi et al. \(2021\)](#) which have spectroscopic redshifts suggesting they are part of the prominent $z = 5.17-5.20$ overdensity discussed here, but which lie outside the ~ 62 arcmin² FRESCO mosaic. These include a QSO at $z \sim 5.18$ ([Barger et al. 2002](#)) and two other galaxies SHARDS20008777 and a source at 12:36:00.0, 62:12:26.1. Nineteen of the plausible 50 sources with redshifts in the range $z = 5.12-5.27$ from [Arrabal Haro et al. \(2018\)](#) lie outside the FRESCO mosaic. Of the 31 sources from [Arrabal Haro et al. \(2018\)](#) which lie in the redshift range $z = 5.12-5.27$ and lie within the FRESCO mosaic, 17 are members of our spectroscopic sample of H α emitters in the redshift range $z = 5.16$ to $z = 5.20$.

With 100 spectroscopic members of the overdensity at $z = 5.17-5.20$, this overdensity is particularly extreme. $\sim 28\%$ of the total number of $z = 5.0-6.0$ H α emitters found over the HDF-North field lie in a $\Delta z \sim 0.03$ interval. This exceeds even the 45 galaxies present in $z \sim 5.4$ overdensity identified over the GOODS-South field ([Helton et al. 2023](#)) and also the 20 galaxy and 24 galaxy overdensities identified at $z \sim 6.19$ and $z \sim 6.33$, respectively, over the J0100+2802 field by [Kashino et al. \(2022\)](#).

Given the much larger number of star-forming galaxies in the immediate vicinity of HDF850.1 than even present over the J0100+2802 field, this may suggest the halo masses associated with this overdensity may be even more extreme than the bright $z \sim 6.33$ QSO J0100+2802 that the EIGER program targeted. In particular, the $z = 5.17-5.20$ overdensity extends over the entire GOODS-North FRESCO field, i.e., a $18 \text{ cMpc} \times 18 \text{ cMpc}$ area and 15 cMpc along the line of sight, which translates to a $4.8 \times 10^3 \text{ cMpc}^3$ comoving volume. Assuming a similar efficiency for line emission across the redshift interval $z = 5.0$ to 6.0 , this translates to an amplitude of $\delta_g + 1 = 8 \pm 1$ for the identified $z = 5.17-5.20$ overdensity.

Interestingly enough, the present overdensity is very similar in comoving size ($17 \text{ cMpc} \times 20 \text{ cMpc} \times 26 \text{ cMpc}$ and $17 \text{ cMpc} \times 20 \text{ cMpc} \times 36 \text{ cMpc}$), volume ($6.7 \times 10^3 \text{ cMpc}^3$ and $1.2 \times 10^4 \text{ cMpc}^3$), and δ_g overdensity factors (4.8 ± 1.8 and 9.5 ± 2.0) to the overdensities at $z = 3.065$ and $z = 3.095$, respectively, identified over the SSA22 field by [Steidel et al. \(1998\)](#) and characterized in more detail by [Topping et al. \(2018\)](#).

3.4.2 Extended Galaxy Structures Around HDF850.1

To gain insight into the extended structures that make up the overdensity at $z = 5.17-5.20$, we constructed a list of candidate extended structures within the FRESCO GOODS-North volume. For this, we

counted the number of galaxies that lie closer than 1.2 cMpc to a given galaxy in the plane of the group and that lie within 10 cMpc along the line of sight, which corresponds to $\Delta z \sim 0.02$ (corresponding to a peculiar velocity of ~ 1000 km/s). We allowed for greater latitude in defining a galaxy structure along the line of sight, given the impact peculiar velocities have on the apparent position of a galaxy in three-dimension space. This list was then ordered from galaxies with the largest number of neighbors in this volume to the smallest number of neighbors. Sources identified as part of richer extended structures were then excluded from structures with a smaller number of members. Finally, extended structures were then combined with adjacent extended structures if their mean centers in the plane of the sky were closer than 3.5 cMpc and their mean redshifts Δz_{mean} differed by 0.005 .

In determining whether to include sources in these extended structures, the 1σ dispersions in the redshifts for each structure are computed excluding sources that are $\Delta z \sim 0.01$ (≈ 500 km/s) from the median redshift for a structure. $\Delta z = 0.01$ is in excess of the redshift dispersion for all of the structures identified here and $\sim 2.9\times$ the median 1σ dispersion. Any source that differs from the median redshift for a structure by $2.5\sigma_z$ is excluded from a structure.

To help illustrate the 3-dimensional spatial distribution of galaxies and extended structures within this $z = 5.17-5.20$ overdensity, we have included Figure 7, which shows four different structures we have identified at $z = 5.170-5.185$ (*left panel*) and four different structures we have identified at $z = 5.185-5.200$ (*center panel*). The rightmost panel shows the redshift distribution of sources in structures 1-4 (*red histogram*) and structures 5-8 (*black histogram*), pointing to the presence of a possible bi-modality in the $z = 5.17-5.20$ overdensity. Additionally, the structures located in the lower redshift mode lie predominantly to the south and western parts of the FRESCO field, while structures in the higher redshift mode, lie predominantly to the north and east.

We also include several additional highly obscured galaxies identified by [Xiao et al. \(2023\)](#) within these overdensities with star-like symbols. Interestingly enough, the same extended structure of galaxies that contains HDF850.1 also features another highly obscured galaxy S3. Additionally, [Xiao et al. \(2023\)](#) report four other highly obscured galaxies in extended structures 1, 6, 7, 11, and 15. The latter galaxy, previously named GN10, was identified as part of earlier work ([Daddi et al. 2009](#); [Riechers et al. 2020](#)).

We have included a full list of the H α emitters in the $z = 5.17-5.20$ overdensity in Table B1 from Appendix B. Galaxies which lie in some nearby overdensities at $z \sim 5.23$, $z \sim 5.27$, and $z \sim 5.3$ over the GOODS North FRESCO field are also presented in this table. In Appendix A, we present the spatial distribution in the plane of the sky of these slightly higher redshift overdensities. The spatial extent of the structures in these overdensities range from 1 cMpc to $4-5 \text{ cMpc}$ in the plane of the sky, much less substantial than we see in the $z = 5.17-5.20$ overdensity that contains HDF850.1, which is the focus of this manuscript.

We include in Table 3 the central coordinates, mean redshift, nominal velocity dispersion, approximate radius, overdensity factor relative to the mean volume density of H α emitters in the GOODS North FRESCO field, and number of member galaxies of these extended structures. The center of each structure is provided both in right ascension and declination and offset from the center of the FRESCO GOODS North field. The median 1σ dispersion in redshift for the extended structures we identified is 0.0035 , while the median velocity dispersion we find is 167^{+12}_{-3} km/s. This is only slightly ($\sim 18 \pm 8\%$) lower than the velocity dispersions [Kashino et al. \(2022\)](#) find, i.e.,

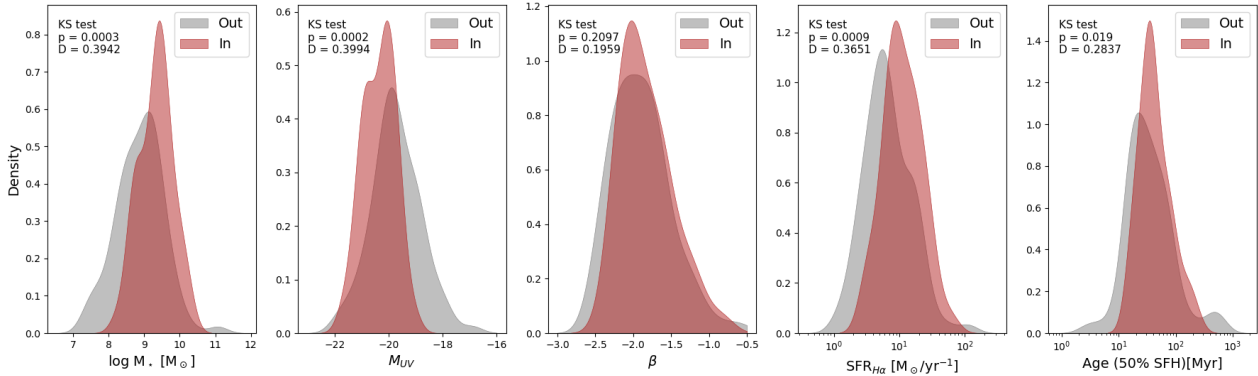


Figure 8. KDE Density plots showing the comparison of Prospector-inferred galaxy properties for sources inside and outside of the overdensity. The "in" sample (red) contains 47 sources between redshifts $z = 5.17$ – 5.20 in the overdensity and identified as part of extended structures, while the "out" sample (grey) contains 86 sources at redshift $z = 4.9$ – 5.5 excluding the overdensity redshift bin and the structures identified with the method detailed in section 3.4.2. Shown in each panel are differences in the fractional cumulative distribution and associated probability that the two distributions are consistent using a Kolomogrov-Smirnov test. The stellar masses, UV luminosities, and star formation rates for galaxies inside the overdensities show a clear shift to higher values than galaxies outside the overdensities.

212 km/s and 197 km/s, for the overdensities in the J0100+2802 field at $z \sim 6.19$ and $z \sim 6.33$, respectively.

Following Long et al. (2020) and Calvi et al. (2021), we also use the stellar masses of the member galaxies to estimate the integrated halo masses of the extended structures that host the galaxies in the extended structures. We do so by computing the total stellar mass we estimate from the member galaxies and then supposing an integrated star formation efficiency of 5% based on detailed studies comparing the galaxy stellar mass functions to the halo mass functions (Behroozi & Silk 2018), but we note that detailed studies (Stefanon et al. 2021b; McLeod et al. 2021) of the ratio of the stellar mass to halo mass density from galaxy stellar mass functions at $z \sim 0$ -10 integrated down to $10^8 M_\odot$ give factors between 0.5% to 2%. We make use of the masses from Naidu et al. (2023, in prep) SED fits with Prospector – except for the sources in the optically-faint samples of Xiao et al. (2023). The derived integrated halo masses range from $10^{10.6} M_\odot$ and $10^{12.6} M_\odot$. Not surprisingly, HDF850.1 and GN10 lie in the halos that belong to the structures with the highest integrated halo masses. Assuming a survey area of ~ 62 arcmin² and $\Delta z \sim 1$ volume ($\sim 2 \times 10^5$ cMpc³), we estimate that the GOODS North FRESCO volume should contain approximately one $10^{12.2} M_\odot$ halo. For this calculation, we made use of the public halo mass function calculator HMFcalc by Murray et al. (2013) adopting a Planck Collaboration et al. (2018) cosmology.

The radius of each extended structure $R_{\text{structure}}$ is computed using the standard formula from Heisler et al. (1985) used in computing dynamical masses of galaxy clusters based on a discrete number of galaxies with measured positions and line-of-sight velocities:

$$R_{\text{structure}} = \frac{\pi N}{2 \sum_{i < j} \frac{1}{R_{\perp ij}}} \quad (3)$$

where N is the number of galaxies in an extended structure and $R_{\perp ij}$ is the projected distance in the plane of the sky between galaxy i and galaxy j .

We also estimate overdensities for the extended structure we identified as part of Table 3 by comparing the volume density of $H\alpha$ emitters within the estimated radius and a $|\Delta z| < 2\sigma_z$ redshift width of an extended structure to that found between $z = 5.0$ to 6.0 for the GOODS-North FRESCO field as a whole. We compute overdensity factors between 8 and 267, far in excess of the linear regime. Based

on the volume density of $H\alpha$ emitters we find in the GOODS North FRESCO volume, i.e., 1.6×10^{-3} cMpc⁻³, we can estimate a nominal bias factor for this population assuming abundance matching and find an average bias factor of ~ 4.7 using the Trenti & Stiavelli (2008) "cosmic variance" calculator. Adjusting for this bias factor, this is suggestive of overdensities in the matter distribution ranging from 2 to 57, which is significantly in excess of ≈ 1 for the linear regime but less than $200\times$ overdensities expected for completely collapsed structures.

It is interesting to ask whether we would expect protoclusters to be present over the FRESCO fields and indeed within the GOODS North FRESCO field. Given that clusters generally have a mass of at least $10^{14} M_\odot$ (e.g. Kravtsov & Borgani 2012) at $z \sim 0$, we can use abundance matching to estimate whether the FRESCO volume contains any such objects. Using the halo mass functions from HMFcalc, we estimate the FRESCO GOODS-North volume to include 4 such clusters with mass $10^{14.0} M_\odot$ and one cluster reaching a mass of $10^{14.4} M_\odot$.

3.4.3 Comparison of Structure Sizes to the Expected Sizes of Protoclusters

We can compare the size of the extended structures we find to that expected from the detailed study of protocluster growth (Chiang et al. 2017) making use of several semi-analytic galaxy formation models (Guo et al. 2013; Henriques et al. 2015) applied to the Millennium simulations (Springel et al. 2005). Chiang et al. (2017) present both the comoving sizes of collapsed protoclusters at various redshifts and the sizes of cosmic volumes that will collapse into $>10^{14} M_\odot$ galaxy clusters by $z \sim 0$. Of relevance, Chiang et al. (2017) find protoclusters to extend to have a comoving radius of ~ 9 cMpc at $z \sim 5.2$, implying overdense structures to extend over a comoving distance of ~ 18 cMpc, very similar to the spatial extent of the overdensities we have identified over the GOODS North FRESCO field (Figure 7). Chiang et al. (2017) suggest that all 10 extended structures identified here likely collapse into a single $>10^{14} M_\odot$ galaxy cluster by $z \sim 0$.

We estimate that the halo masses of the most massive collapsed halo in those extended structures would be $10^{12.0} M_\odot$ and $10^{12.2} M_\odot$, respectively, at $z \sim 5.2$. Assuming that average overdensity factor in the collapsed halos is 200, the size of the halos would be 0.3

cMpc and 0.4 cMpc at $z \sim 5.2$, i.e., 8" to 13" in the plane of the sky. In computing a radius of the identified structures, the above equation gives greater weight to galaxy pairs that have smaller separations. The fact that many of these extended structures have computed sizes not especially larger than 0.4 cMpc suggests that at least a few of the member galaxies in the extended structures are part of the same halos.

3.4.4 Characteristics of Galaxies in the $z = 5.17$ -5.20 Overdensity vs. Those Outside

To put the extreme properties of HDF850.1 in context, we use the SED-fitting code *Prospector* (Leja et al. 2017b; Johnson et al. 2021) to derive galaxy properties from our extensive spectroscopically confirmed sample of galaxies in FRESKO GOODS-North. Our *Prospector* fits use FSPS with the MIST stellar models. We do not fit for redshift and set it to the derived z_{grism} value inferred by our pipeline using *grizli*. Along with the photometry, fluxes from emission lines identified in the Grism 1D spectra are also used as an input. We make use of *Prospector*'s more flexible non-parametric star-formation history (SFH) with 8 bins evenly separated in lookback time with a "continuity" prior for smoother SFH. The output catalog contains all sources detected in the detection image that were visually inspected by at least one member of the FRESKO team along with the inferred properties from SED-fitting such as the retained stellar mass M_{\star} , UV slope β , star formation rates SFR or age at 50 % of the total stellar mass.

To highlight the distinct properties galaxies may have within the overdensity or its structures and outside of it, we compare two samples. One contains all the galaxies in the $z = 5.17$ -5.20 overdensity that have been identified as being part of a structure ("in" with 40 sources) while the second sample contains all the remaining galaxies from $z = 4.9$ to $z = 5.5$ not identified in such structures ("out" with 86) and also excluding the redshift bin $z = 5.17$ -5.20. We also apply a magnitude cut of 27 AB mag in F182M. While this will limit our inferences to galaxies intrinsically brighter than -20 mag, this choice was made to alleviate the uncertainties on the inferred parameters from faint sources – particularly for stellar masses – and avoid a bias towards strong $H\alpha$ emitters only. We report the output of the *Prospector* fits for these two samples with kernel density estimate (KDE) plots as shown in Figure 8. We also compare SFRs inferred from $H\alpha$ using Eq. 1. We use the $H\alpha$ flux corrected for dust attenuation with the empirical relation linking it to β slopes from Shivaei et al. (2020). Finally, we use a two-sample Kolmogorov-Smirnov (KS) test to comment on the dissimilarities in our selection of sources.

Based on the sizes of our two samples, we require a critical D-value of 0.3311 to demonstrate at 99.5% confidence ($\alpha = 0.005$) that the distributions of the properties for sources inside and outside overdensities are different. While we do not find a clear differences (at 99.5% confidence) in the distributions for β slopes and ages at 50% of the SFH, the D-values and p-values for the masses and ages show clear differences between the two populations of galaxies at this redshift. Our results suggest that the galaxies in the overdensity are more evolved, more massive and with higher SFRs than the galaxies outside of these structures. The median stellar mass M_{\star} in the overdensity is $\sim 2.5 \times 10^9 M_{\odot}$ vs. $\sim 8 \times 10^8 M_{\odot}$ for the galaxies outside, a factor of ~ 3 difference. Earlier work by Steidel et al. (2005) had shown that the masses and ages of galaxies in a similarly prominent (i.e. $\delta_g \sim 7$) overdensity at $z = 2.3$ were twice as high as those outside the overdensity in line with our results.

More evidence from FRESKO for the most extreme sources being found in overdense environments can be found in the Xiao et al. (2023) $H\alpha$ selection of highly obscured sources over the GOODS North field. In particular, the five $z = 4.9$ -6.6 sources with the highest estimated stellar masses and SFRs all lie within the overdensities at $z \sim 5.16$ -5.20 and $z \sim 5.30$.

4 UTILITY OF WIDE-AREA GRISM SURVEYS FOR MAPPING THE BUILD-UP OF DUST-OBSCURED GALAXIES AT $Z > 5$

The identification of a 13σ $H\alpha$ emission line in the well-known dust-obscured galaxy HDF850.1 clearly demonstrates the enormous utility of the NIRCcam grism for deriving redshifts for dust-obscured galaxies at $z > 4$ and mapping out the build-up of these galaxies from early times.

Another particularly exciting example of such a source as relates to HDF850.1 is shown in Figure 9 and been given a source ID S3. That source has a redshift $z = 5.179$ derived from the detection of both $H\alpha$ ($>20\sigma$) and the [SII]_{6719,6730} doublet ($\sim 9\sigma$; Xiao et al. 2023). Given the similar redshift and spatial proximity, S3 appears to be part of the same extended structure as HDF850.1. Remarkably, this source shows even more extreme stellar masses and SFRs than HDF850.1 (Xiao et al. 2023).

Earlier, Oesch et al. (2023) presented a third example of such a highly obscured source with a detected $H\alpha$ line in their Figure 10. In parallel with the current study, Xiao et al. (2023) present a much larger sample of obscured, $H\alpha$ emitters at $z > 5$, leveraging the FRESKO NIRCcam grism data to derive spectroscopic redshifts.

The existence of large numbers of obscured galaxies with detectable $H\alpha$ emission may arise because of prevalent merging activity amongst the brightest far-IR sources (e.g. Clements et al. 1996; Tacconi et al. 2008) and the possibility that the merging activity could create less obscured sight lines by which $H\alpha$ photons could escape from galaxies (e.g., Le Reste et al. 2023). One of the components in a merging system might also be subject to substantially less dust obscuration, which would also enhance the detectability of IR luminous sources. Note that many ultra-luminous far-IR bright galaxies at $z \sim 1$ -3 even reveal the presence of escaping Lyman- α photons (e.g. Chapman et al. 2003, 2005) through sensitive rest-UV spectroscopy. Given the utility of the Ly α line, the ubiquity of $H\alpha$ line emission from $z > 5$ ULIRGs is thus less surprising.

Of course, the non-detection of $H\alpha$ in the rather extreme star-forming source SPT0311-58 at $z = 6.900$ with MIRI and the present non-detection of the northern component to HDF850.1 suggests that not every highly obscured source will be well detected in $H\alpha$ (Álvarez-Márquez et al. 2023b) in NIRCcam grism observations, but the detection of $H\alpha$ at high significance ($>10\sigma$) from the southern component to HDF850.1, GN10, and a handful of other far-IR luminous galaxies with the FRESKO grism observations (Xiao et al. 2023) suggests that the selection of dusty star-forming galaxies could be moderately complete in very wide-area grism observations.

Given the identification of 7 highly obscured galaxies populating the $z = 5.15$ -5.32 structures over the GOODS North FRESKO field (Xiao et al. 2023), the extension of such a survey over much wider areas, e.g., $>600 \text{ arcmin}^2$, has the potential to identify >70 obscured far-IR bright star-forming galaxies at $z > 5$ while simultaneously allowing for a characterization of the structures in which the massive galaxies are forming.

Such a survey would yield even more far-IR luminous galaxies at $z > 5$ than even the ≈ 42 (707 sources $\times \approx 6\%$ at $z > 4$) far-IR

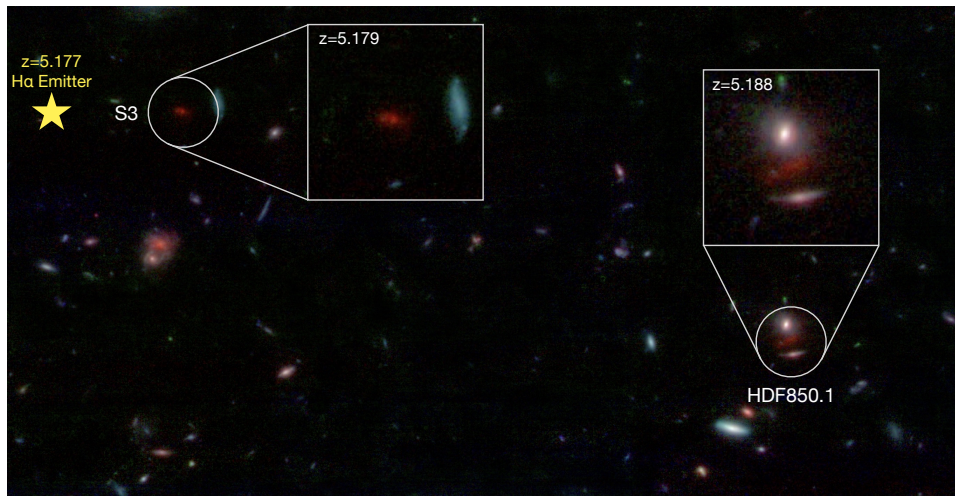


Figure 9. (*upper panels*) Color composite image of another highly obscured star-forming source S3 at $z = 5.179$ in the same extended structure #3 as HDF850.1, as seen in a false color image ($60'' \times 30''$) made with the *JWST* NIRCcam F182M, F210M, F444W data. The redshift $z = 5.179$ of this source is based on the detection of both $H\alpha$ ($>20\sigma$) and the $[\text{SII}]_{6719,6730}$ doublet ($\sim 9\sigma$) in the FRESCO grism data. Another $H\alpha$ emitter (ID 3946) at $z = 5.177$ from the same extended structure (indicated with the yellow star) also lies within this same footprint and could reside in the same dark matter halo as S3 (being separated by $7''$ [or 0.26 cMpc] in the plane of the sky). Redshift measurements have been obtained for a large number of other highly obscured galaxies over the ~ 124 arcmin 2 FRESCO mosaic using detected $H\alpha$ lines (Xiao et al. 2023), with typical S/N's of >10 for the sources with the highest inferred SFRs. The detection of $H\alpha$ line emission from sources like HDF850.1 and S3 – and many similarly dust-obscured and high-SFR sources – shows the huge potential wide-area NIRCcam grism observations have for mapping the build-up of massive, dust-enshrouded star forming galaxies in the early universe.

bright galaxies estimated to be identified at $z > 4$ (Dudzevičiūtė et al. 2020) over the 1 deg 2 AS2UDS program (Stach et al. 2019). Such a program would yield many IR-bright sources at $z > 4$ than the ≈ 4 far-IR bright galaxies identified over 184 arcmin 2 from the 2mm MORA program (Casey et al. 2021). Even scaling a MORA-like program to 600 arcmin 2 would only result in a yield of ≈ 13 $z > 4$ galaxies.

5 SUMMARY

In this paper, we present the detection of a 13σ $H\alpha$ line for HDF850.1 in the NIRCcam F444W grism observations over the GOODS North field from FRESCO (Oesch et al. 2023), recovering a redshift of 5.188 ± 0.001 . Detection of $H\alpha$ in HDF850.1 is particularly noteworthy, given how obscured star formation from the source is. HDF850.1 was one of the first submm galaxies to be identified with SCUBA (Hughes et al. 1998) and evaded efforts to pin down its redshift for >10 years until the Plateau de Bure Interferometer secured the detection of [CII] and various CO lines from a spectral scan (Walter et al. 2012).

In addition, HDF850.1 is clearly detected in the F444W imaging observations available over the source with NIRCcam, with the emission segregated into a distinct northern and southern component. These two distinct components were also evident in the earlier observations of [CII] from HDF850.1 with PdBI (Neri et al. 2014). Modeling the SEDs of the two components of HDF850.1 based on the available HST + NIRCcam F182M, F210M, and F444W imaging observations, we find a much higher SFR, stellar mass, and dust obscuration for the northern component than the southern component.

The majority of the $H\alpha$ emission for HDF850.1 appears consistent with originating from the southern component, not only due to the spatial localization of the emission but also due to its showing a very similar $\Delta v \sim 130$ km/s velocity offset to that seen in the southern component from [CII] emission (Neri et al. 2014). Comparison of

the SFR inferred from the observed $H\alpha$ emission with that seen from [CII] is suggestive of the $H\alpha$ emission from the southern component being $93 \pm 3\%$ attenuated and the northern component $>98\%$ attenuated.

Leveraging redshift determinations possible from the FRESCO NIRCcam grism observations in F444W over the GOODS North field, we note the existence of 100 galaxies in total in the $z = 5.17-5.20$ interval, indicative of a huge $8\times$ overdensity of galaxies in that redshift interval relative to the $z = 5.0-6.0$ population of $H\alpha$ emitters we see over GOODS North. Earlier work by Walter et al. (2012), Arrabal Haro et al. (2018), and Calvi et al. (2021) had previously demonstrated the existence of a substantial overdensity around HDF850.1, but with a much smaller number of spectroscopically confirmed sources than we find as part of this study.

Taking advantage of both the spatial and redshift information we have of galaxies in the $z = 5.17-5.20$ and slightly higher redshift ($z = 5.22-5.31$) overdensities, we have organized sources into 18 extended structures and computed radii, masses, velocity dispersions for the structures. The median 1σ dispersion in the identified structures in redshift and v_{los} is 0.0035 and 167 km/s, which is only slightly ($18 \pm 8\%$) lower than what Kashino et al. (2022) find for the extended structures in the J0100+2802 field at $z \sim 6.19$ and $z \sim 6.33$.

Interestingly, the comoving physical size of the extended structures we find around HDF850.1 extend over a 18 cMpc \times 18 cMpc \times 15 cMpc volume, very similar to the ~ 18 cMpc physical size Chiang et al. (2017) expect for protoclusters based on an analysis of various semi-analytic galaxy formation results building on the Millennium simulation (Springel et al. 2005: §3.4.3). The link to the $z = 5.17-5.20$ overdensity being the progenitor to a $>10^{14} M_{\odot}$ $z \sim 0$ galaxy cluster is further strengthened by noting that within the FRESCO GOODS North volume we would expect four $>10^{14} M_{\odot}$ clusters and one $>10^{14.4} M_{\odot}$ cluster to form by $z \sim 0$.

Additionally, we have made a systematic comparison of galaxy masses, SFRs, UV luminosities, ages, and apparent dust extinctions inside the $z = 5.17-5.20$ overdensity to that outside the $z = 5.17-$

5.20 overdensity and other overdensities in the field. We find strong evidence ($>3\sigma$) that galaxies inside the overdensities have higher stellar masses, SFRs, and UV luminosities than those outside these overdensities. This conclusion is strengthened by the inclusion of optically faint, massive, high-SFR dust-obscured galaxies at $z = 5.0$ - 6.0 , almost all of which lie inside some overdensity within the GOODS North.

In the future, it should be possible to significantly expand the number of dusty star-forming galaxies identified in the $z > 5$ universe thanks to on-going NIRCcam grism observations from EIGER (Kashino et al. 2022), ASPIRE (Wang et al. 2023), a new NIRCcam grism program from MIRI GTO team over GOODS South (program ID 4549), as well as deeper NIRCcam grism observations approved over a deep NIRCcam parallel field (program ID 4540) and various HFF clusters (program ID 2883, 3516, 3538). Of course, to obtain the strongest constraints, a substantially wider area NIRCcam program would be ideal, especially over areas that already have sensitive observations of the far-IR continuum as has been obtained by the ASPIRE program over clusters (Wang et al. 2023), the ALMA GOODS program obtained over the CANDELS Deep region of the GOODS South (Franco et al. 2020), and ex-MORA program over the COSMOS field (Casey et al. 2021).

ACKNOWLEDGEMENTS

We are grateful to Roberto Neri and collaborators for providing us with spatially resolved information on both the dust-continuum and [CII] line emission from their high spatial resolution PdBI observations. RJB acknowledges support from NWO grants 600.065.140.11N211 (vrij competitie) and TOP grant TOP1.16.057. The Cosmic Dawn Center (DAWN) is funded by the Danish National Research Foundation under grant No. 140. Cloud-based data processing and file storage for this work is provided by the AWS Cloud Credits for Research program. Support for this work was provided by NASA through grant JWST-GO-01895 awarded by the Space Telescope Science Institute, which is operated by the Association of Universities for Research in Astronomy, Inc., under NASA contract NAS 5-26555. RPN acknowledges funding from JWST programs GO-1933 and GO-2279. Support for this work was provided by NASA through the NASA Hubble Fellowship grant HST-HF2-51515.001-A awarded by the Space Telescope Science Institute, which is operated by the Association of Universities for Research in Astronomy, Incorporated, under NASA contract NAS5-26555. MS acknowledges support from the CIDEAGENT/2021/059 grant, from project PID2019-109592GB-I00/AEI/10.13039/501100011033 from the Spanish Ministerio de Ciencia e Innovación - Agencia Estatal de Investigación. This study forms part of the Astrophysics and High Energy Physics programme and was supported by MCIN with funding from European Union NextGenerationEU (PRTR-C17.11) and by Generalitat Valenciana under the project n. ASFAE/2022/025. RAM acknowledges support from the ERC Advanced Grant 740246 (Cosmic_Gas) and the Swiss National Science Foundation through project grant 200020_207349.

This work is based on observations made with the NASA/ESA/CSA James Webb Space Telescope. The data were obtained from the Mikulski Archive for Space Telescopes at the Space Telescope Science Institute, which is operated by the Association of Universities for Research in Astronomy, Inc., under NASA contract NAS 5-03127 for JWST. These observations are associated with program # 1895.

This paper made use of several publicly available software pack-

ages. We are indebted to the respective authors for their work: IPython (Pérez & Granger 2007), matplotlib (Hunter 2007), numpy (Oliphant 2015), scipy (Virtanen et al. 2020), jupyter (Kluyver et al. 2016), Astropy (Astropy Collaboration et al. 2013, 2018), grizli (v1.7.11; Brammer 2018; Brammer et al. 2022), EAZY (Brammer et al. 2008), SExtractor (Bertin & Arnouts 1996).

DATA AVAILABILITY

All data used here are available from the Barbara A. Mikulski Archive for Space Telescopes (MAST: <https://mast.stsci.edu>), both in the form of raw and high level science products.

REFERENCES

- Álvarez-Márquez J., et al., 2023a, *A&A*, 671, A105
 Álvarez-Márquez J., et al., 2023b, *A&A*, 671, A105
 Arrabal Haro P., et al., 2018, *MNRAS*, 478, 3740
 Astropy Collaboration et al., 2013, *A&A*, 558, A33
 Astropy Collaboration et al., 2018, *AJ*, 156, 123
 Barger A. J., Cowie L. L., Brandt W. N., Capak P., Garmire G. P., Hornschemeier A. E., Steffen A. T., Wehner E. H., 2002, *AJ*, 124, 1839
 Behroozi P., Silk J., 2018, *MNRAS*, 477, 5382
 Bertin E., Arnouts S., 1996, *A&AS*, 117, 393
 Béthermin M., et al., 2020, *A&A*, 643, A2
 Bouwens R. J., et al., 2021, *AJ*, 162, 47
 Bouwens R. J., et al., 2022, *ApJ*, 931, 160
 Brammer G., 2018, Gbrammer/Grizli: Preliminary Release, Zenodo, doi:10.5281/zenodo.1146905
 Brammer G. B., van Dokkum P. G., Coppi P., 2008, *ApJ*, 686, 1503
 Brammer G., Strait V., Matharu J., Momcheva I., 2022, grizli, Zenodo, doi:10.5281/zenodo.6672538
 Bruzual G., Charlot S., 2003, *MNRAS*, 344, 1000
 Calvi R., Dannerbauer H., Arrabal Haro P., Rodríguez Espinosa J. M., Muñoz-Tuñón C., Pérez González P. G., Geier S., 2021, *MNRAS*, 502, 4558
 Casey C. M., et al., 2021, *ApJ*, 923, 215
 Chabrier G., 2003, *Publications of the Astronomical Society of the Pacific*, 115, 763
 Chapman S. C., Blain A. W., Ivison R. J., Smail I. R., 2003, *Nature*, 422, 695
 Chapman S. C., Blain A. W., Smail I., Ivison R. J., 2005, *ApJ*, 622, 772
 Chiang Y.-K., Overzier R. A., Gebhardt K., Henriques B., 2017, *ApJ*, 844, L23
 Clements D. L., Sutherland W. J., McMahon R. G., Saunders W., 1996, *MNRAS*, 279, 477
 Cowie L. L., Barger A. J., Wang W. H., Williams J. P., 2009, *ApJ*, 697, L122
 Daddi E., Dannerbauer H., Krips M., Walter F., Dickinson M., Elbaz D., Morrison G. E., 2009, *ApJ*, 695, L176
 Davidzon I., et al., 2017, *A&A*, 605, A70
 Dayal P., et al., 2022, *MNRAS*, 512, 989
 Dojčinović I., Kovačević-Dojčinović J., Popović L. Č., 2023, *Advances in Space Research*, 71, 1219
 Downes D., et al., 1999, *A&A*, 347, 809
 Dudzevičiūtė U., et al., 2020, *MNRAS*, 494, 3828
 Dunlop J. S., et al., 2004, *MNRAS*, 350, 769
 Erb D. K., et al., 2014, *ApJ*, 795, 33
 Faisst A. L., et al., 2020, *ApJS*, 247, 61
 Franco M., et al., 2020, *A&A*, 643, A53
 Freeman W. R., et al., 2019, *ApJ*, 873, 102
 Gialalisco M., et al., 2004, *ApJ*, 600, L93
 Grogin N. A., et al., 2011, *ApJS*, 197, 35
 Guo Q., White S., Angulo R. E., Henriques B., Lemson G., Boylan-Kolchin M., Thomas P., Short C., 2013, *MNRAS*, 428, 1351
 Harikane Y., et al., 2022, *ApJ*, 929, 1
 Heisler J., Tremaine S., Bahcall J. N., 1985, *ApJ*, 298, 8
 Helton J. M., et al., 2023, *arXiv e-prints*, p. arXiv:2302.10217

- Henriques B. M. B., White S. D. M., Thomas P. A., Angulo R., Guo Q., Lemson G., Springel V., Overzier R., 2015, *MNRAS*, **451**, 2663
- Hughes D. H., et al., 1998, *Nature*, **394**, 241
- Hunter J. D., 2007, *Computing In Science & Engineering*, **9**, 90
- Illingworth G., et al., 2016, arXiv e-prints, p. arXiv:1606.00841
- Johnson B. D., Leja J., Conroy C., Speagle J. S., 2021, *ApJS*, **254**, 22
- Kashino D., Lilly S. J., Matthee J., Eilers A.-C., Mackenzie R., Bordoloi R., Simcoe R. A., 2022, arXiv e-prints, p. arXiv:2211.08254
- Kennicutt R. C., Evans N. J., 2012, *ARA&A*, **50**, 531
- Kewley L. J., Dopita M. A., Leitherer C., Davé R., Yuan T., Allen M., Groves B., Sutherland R., 2013, *ApJ*, **774**, 100
- Kluyver T., et al., 2016, in Loizides F., Schmidt B., eds, *Positioning and Power in Academic Publishing: Players, Agents and Agendas*. pp 87 – 90
- Koekemoer A. M., et al., 2011, *ApJS*, **197**, 36
- Kravtsov A. V., Borgani S., 2012, *ARA&A*, **50**, 353
- Kroupa P., Weidner C., 2003, *ApJ*, **598**, 1076
- Le Fèvre O., et al., 2020, *A&A*, **643**, A1
- Le Reste A., et al., 2023, arXiv e-prints, p. arXiv:2301.02676
- Leja J., Johnson B. D., Conroy C., van Dokkum P. G., Byler N., 2017a, *ApJ*, **837**, 170
- Leja J., Johnson B. D., Conroy C., van Dokkum P. G., Byler N., 2017b, *ApJ*, **837**, 170
- Long A. S., et al., 2020, *ApJ*, **898**, 133
- Madau P., Dickinson M., 2014, *ARA&A*, **52**, 415
- Matthee J., et al., 2023, arXiv e-prints, p. arXiv:2306.05448
- McLeod D. J., McLure R. J., Dunlop J. S., Cullen F., Carnall A. C., Duncan K., 2021, *MNRAS*, **503**, 4413
- Murray S. G., Power C., Robotham A. S. G., 2013, *Astronomy and Computing*, **3**, 23
- Neri R., Downes D., Cox P., Walter F., 2014, *A&A*, **562**, A35
- Oesch P. A., et al., 2023, arXiv e-prints, p. arXiv:2304.02026
- Oke J. B., Gunn J. E., 1983, *ApJ*, **266**, 713
- Oliphant T. E., 2015, *Guide to NumPy*. Continuum Press
- Peng C. Y., Ho L. C., Impey C. D., Rix H.-W., 2002, *AJ*, **124**, 266
- Pérez F., Granger B. E., 2007, *Computing in Science and Engineering*, **9**, 21
- Perrin M. D., Sivaramakrishnan A., Lajoie C.-P., Elliott E., Pueyo L., Ravindranath S., Albert L., 2014, in Oschmann Jacobus M. J., Clampin M., Fazio G. G., MacEwen H. A., eds, *Society of Photo-Optical Instrumentation Engineers (SPIE) Conference Series Vol. 9143, Space Telescopes and Instrumentation 2014: Optical, Infrared, and Millimeter Wave*. p. 91433X, doi:10.1117/12.2056689
- Planck Collaboration et al., 2018, arXiv e-prints, p. arXiv:1807.06209
- Reddy N. A., Steidel C. C., Erb D. K., Shapley A. E., Pettini M., 2006, *ApJ*, **653**, 1004
- Reddy N. A., Steidel C. C., Pettini M., Adelberger K. L., Shapley A. E., Erb D. K., Dickinson M., 2008, *ApJS*, **175**, 48
- Reddy N. A., Topping M. W., Sanders R. L., Shapley A. E., Brammer G., 2023, *ApJ*, **948**, 83
- Richards E. A., 1999, *ApJ*, **513**, L9
- Riechers D. A., et al., 2020, *ApJ*, **895**, 81
- Robertson B. E., 2022, *ARA&A*, **60**, 121
- Schaerer D., et al., 2020, *A&A*, **643**, A3
- Shapley A. E., et al., 2015, *ApJ*, **801**, 88
- Shivaei I., et al., 2020, *ApJ*, **899**, 117
- Smail I., et al., 2021, *MNRAS*, **502**, 3426
- Springel V., et al., 2005, *Nature*, **435**, 629
- Stach S. M., et al., 2019, *MNRAS*, **487**, 4648
- Stefanon M., Bouwens R. J., Labbé I., Illingworth G. D., Gonzalez V., Oesch P. A., 2021a, *ApJ*, **922**, 29
- Stefanon M., Bouwens R. J., Labbé I., Illingworth G. D., Gonzalez V., Oesch P. A., 2021b, *ApJ*, **922**, 29
- Steidel C. C., Adelberger K. L., Dickinson M., Giavalisco M., Pettini M., Kellogg M., 1998, *ApJ*, **492**, 428
- Steidel C. C., Adelberger K. L., Shapley A. E., Erb D. K., Reddy N. A., Pettini M., 2005, *ApJ*, **626**, 44
- Tacconi L. J., et al., 2008, *ApJ*, **680**, 246
- Tang M., et al., 2023, arXiv e-prints, p. arXiv:2301.07072
- Topping M. W., Shapley A. E., Steidel C. C., Naoz S., Primack J. R., 2018, *ApJ*, **852**, 134
- Trenti M., Stiavelli M., 2008, *ApJ*, **676**, 767
- Virtanen P., et al., 2020, *Nature Methods*, **17**, 261
- Wagg J., Hughes D. H., Aretxaga I., Chapin E. L., Dunlop J. S., Gaztañaga E., Devlin M., 2007, *MNRAS*, **375**, 745
- Walter F., et al., 2012, *Nature*, **486**, 233
- Wang F., et al., 2023, *ApJ*, **951**, L4
- Weiner B. J., AGHAST Team 2014, in American Astronomical Society Meeting Abstracts #223. p. 227.07
- Whitaker K. E., Pope A., Cybulski R., Casey C. M., Popping G., Yun M. S., 2017, *ApJ*, **850**, 208
- Whitaker K. E., et al., 2019, *ApJS*, **244**, 16
- Xiao M., et al., 2023, arXiv e-prints, p. arXiv:2309.02492
- da Cunha E., Charlot S., Elbaz D., 2008, *MNRAS*, **388**, 1595
- da Cunha E., et al., 2015, *ApJ*, **806**, 110

APPENDIX A: EXTENDED GALAXY STRUCTURES AT $Z \sim 5.22$ -5.31

For completeness and as an illustration of the extended galaxy structures that exist at redshift just above the prominent $z = 5.17$ -5.20 overdensity. Similar to Figure 7 from the main text, we show the spatial distribution of galaxies in the galaxy overdensities at the slightly higher redshifts of $z \sim 5.23$, $z \sim 5.27$, and $z \sim 5.30$ for context. As in the main text, we have segregated sources in the overdensities into different structures using the same approach as described in §3.4.2.

While in some cases these overdensities consist of just a single group of ~ 3 -10 galaxies lying within 1 cMpc of each other (e.g., structures 9, 15), in other cases the overdensities extend over larger (~ 3 -5 cMpc) scales. However, even for the most extended structures in these overdensities, galaxies in these overdensities are much less spatially extended than in the prominent $z = 5.17$ -5.20 overdensity that is the focus of this study.

APPENDIX B: $H\alpha$ EMITTERS IDENTIFIED IN THE $Z \sim 5.15$ -5.31 OVERDENSITY OVER THE GOODS NORTH FRESCO FIELD

In this appendix, we provide a full catalog of the star-forming galaxies identified as part of the prominent $z = 5.15$ -5.31 overdensity over the GOODS North FRESCO field. Coordinates for individual sources in the overdensity, together with their redshift determinations, flux measurements in the F210M band, $H\alpha$ fluxes, stellar masses, SFRs, UV-continuum slopes, and V-band dust attenuations are provided in Table B1. Also indicated are whether sources were previously reported as part of the Walter et al. (2012), Arrabal Haro et al. (2018), Riechers et al. (2020), Calvi et al. (2021), or Matthee et al. (2023) studies. Given the $\Delta z \sim 0.07$ uncertainties in the photometric redshifts derived as part of Arrabal Haro et al. (2018), sources in Arrabal Haro et al. (2018) are considered to be likely members of the overdensity at $z \sim 5.2$ if their photometry redshifts are $z > 5.13$ and $z < 5.27$.

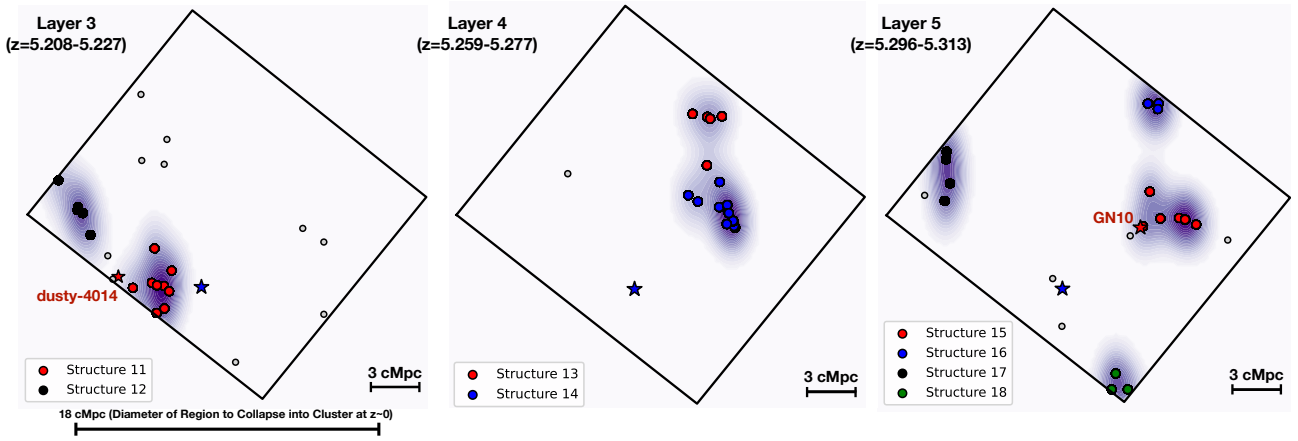


Figure A1. Similar to Figure 7 but for the identified structures in the overdensities of star-forming galaxies we have identified over the GOODS North FRESCO field at $z \sim 5.22$, $z \sim 5.27$, and $z \sim 5.30$. The red star indicates the position of Dusty-4014 (dust-obscured galaxy identified by Matthee et al. 2023 and Xiao et al. 2023 showing H α in emission) and GN10 (Daddi et al. 2009; Riechers et al. 2020). The spatial extent of the substructures range from 1 cMpc to 4 cMpc in size.

Table B1. Catalogs of Star-Forming Galaxies at $z \sim 5.15$ -5.32 that are part of the overdensity in the FRESKO GOODS North Field.

ID	RA	DEC	z_{spec}^a	m_{210} [mag]	$f_{H\alpha}$ [10^{-18} ergs/s/cm 2]	$\log(M_{\star})$	β	A_V	SFR	Ref b
Extended Structure 1										
2152	12:36:25.39	62:11:19.8	5.161	25.6	15.0 ± 0.3	$9.57^{+0.25}_{-0.49}$	$-1.27^{+0.15}_{-0.11}$	$0.53^{+0.14}_{-0.23}$	$31.5^{+45.1}_{-15.4}$	
2096	12:36:24.97	62:11:18.2	5.163	25.7	5.3 ± 0.4	$9.79^{+0.18}_{-0.27}$	$-1.52^{+0.23}_{-0.20}$	$0.50^{+0.23}_{-0.17}$	$37.5^{+72.0}_{-25.9}$	
Dusty-1257 b	12:36:24.68	62:11:17.0	5.167	25.9	7.6 ± 0.3	$>9.7^c$	— c	— c	— c	[6]
Extended Structure 2										
8619	12:36:27.98	62:13:19.9	5.165	28.3	1.4 ± 0.2	$8.40^{+0.38}_{-0.31}$	$-1.96^{+0.27}_{-0.17}$	$0.81^{+0.14}_{-0.26}$	$2.0^{+2.9}_{-1.4}$	
10338	12:36:30.69	62:13:44.0	5.172	28.4	1.2 ± 0.1	$7.40^{+0.31}_{-0.13}$	$-2.38^{+0.18}_{-0.11}$	$0.90^{+0.04}_{-0.06}$	$0.5^{+0.5}_{-0.1}$	
10351	12:36:30.63	62:13:44.1	5.173	27.3	1.9 ± 0.2	$8.65^{+0.26}_{-0.23}$	$-2.02^{+0.10}_{-0.10}$	$0.69^{+0.14}_{-0.22}$	$7.0^{+5.2}_{-2.8}$	
9967	12:36:31.37	62:13:39.0	5.173	27.8	2.4 ± 0.2	$8.42^{+0.21}_{-0.68}$	$-2.15^{+0.12}_{-0.14}$	$0.61^{+0.24}_{-0.30}$	$3.0^{+5.9}_{-2.1}$	
9247	12:36:28.75	62:13:30.0	5.174	27.8	1.3 ± 0.2	$8.36^{+0.61}_{-0.23}$	$-2.20^{+0.08}_{-0.07}$	$0.84^{+0.12}_{-0.48}$	$3.5^{+6.1}_{-1.9}$	
8799	12:36:33.73	62:13:22.9	5.175	27.2	1.7 ± 0.2	$8.82^{+0.18}_{-0.30}$	$-2.02^{+0.12}_{-0.09}$	$0.56^{+0.26}_{-0.16}$	$8.2^{+9.3}_{-4.4}$	
9982	12:36:31.98	62:13:39.0	5.178	25.0	13.0 ± 0.4	$10.07^{+0.17}_{-0.53}$	$-1.52^{+0.12}_{-0.13}$	$0.57^{+0.26}_{-0.15}$	$38.4^{+31.6}_{-18.2}$	
5848	12:36:37.52	62:12:36.0	5.179	26.1	5.5 ± 0.3	$9.41^{+0.27}_{-0.15}$	$-1.69^{+0.08}_{-0.09}$	$0.53^{+0.26}_{-0.18}$	$27.3^{+24.4}_{-23.6}$	[1,2]
8586	12:36:35.87	62:13:19.1	5.179	25.8	2.6 ± 0.4	$9.44^{+0.25}_{-0.63}$	$-2.14^{+0.10}_{-0.10}$	$0.70^{+0.14}_{-0.28}$	$19.7^{+8.7}_{-14.5}$	
9754	12:36:31.83	62:13:36.2	5.179	26.5	4.7 ± 0.2	$9.16^{+0.33}_{-0.32}$	$-2.02^{+0.10}_{-0.08}$	$0.35^{+0.28}_{-0.18}$	$27.9^{+30.8}_{-14.5}$	
10431	12:36:30.22	62:13:45.0	5.180	25.5	8.8 ± 0.3	$9.65^{+0.18}_{-0.38}$	$-1.69^{+0.09}_{-0.10}$	$0.56^{+0.15}_{-0.14}$	$39.0^{+37.9}_{-17.7}$	
10723	12:36:29.11	62:13:49.0	5.181	27.6	1.5 ± 0.2	$8.14^{+0.20}_{-0.21}$	$-2.46^{+0.09}_{-0.08}$	$0.95^{+0.03}_{-0.10}$	$2.5^{+1.3}_{-0.9}$	
15198	12:36:28.23	62:14:39.6	5.181	27.0	2.6 ± 0.2	$8.96^{+0.17}_{-0.49}$	$-2.05^{+0.08}_{-0.09}$	$0.64^{+0.20}_{-0.22}$	$10.1^{+14.4}_{-6.8}$	
9362	12:36:32.49	62:13:31.3	5.181	25.6	8.9 ± 0.3	$9.51^{+0.12}_{-0.26}$	$-2.15^{+0.09}_{-0.06}$	$0.47^{+0.19}_{-0.19}$	$60.6^{+33.6}_{-25.6}$	
8576	12:36:28.07	62:13:19.5	5.182	26.7	5.1 ± 0.2	$9.11^{+0.16}_{-0.13}$	$-1.89^{+0.10}_{-0.12}$	$0.51^{+0.16}_{-0.11}$	$21.3^{+11.2}_{-10.2}$	
Extended Structure 3										
5578	12:37:06.17	62:12:30.7	5.172	27.8	1.3 ± 0.2	$8.43^{+0.19}_{-0.24}$	$-2.06^{+0.14}_{-0.12}$	$0.74^{+0.16}_{-0.28}$	$4.2^{+3.1}_{-1.7}$	
7709	12:36:59.75	62:13:06.1	5.173	27.0	2.9 ± 0.3	$8.87^{+0.20}_{-0.30}$	$-1.88^{+0.12}_{-0.12}$	$0.58^{+0.17}_{-0.11}$	$9.4^{+7.2}_{-4.4}$	
3946	12:36:57.24	62:12:00.8	5.177	26.7	2.0 ± 0.3	$8.93^{+0.55}_{-0.43}$	$-1.55^{+0.15}_{-0.12}$	$0.61^{+0.10}_{-0.09}$	$7.0^{+10.0}_{-3.6}$	
6654	12:36:57.28	62:12:49.3	5.178	26.5	2.0 ± 0.3	$8.87^{+0.31}_{-0.20}$	$-2.19^{+0.07}_{-0.07}$	$0.89^{+0.07}_{-0.14}$	$8.7^{+6.8}_{-3.3}$	[2]
S3	12:36:56.56	62:12:07.4	5.179	28.2	5.3 ± 0.3	$>9.7^c$	— c	— c	— c	[6]
5286	12:36:50.32	62:12:26.1	5.180	26.4	5.0 ± 0.3	$8.78^{+0.20}_{-0.16}$	$-2.08^{+0.12}_{-0.08}$	$0.70^{+0.13}_{-0.13}$	$9.7^{+5.0}_{-2.9}$	
6557	12:36:49.86	62:12:47.7	5.180	25.8	7.9 ± 0.4	$9.69^{+0.23}_{-0.61}$	$-1.48^{+0.12}_{-0.11}$	$0.55^{+0.25}_{-0.17}$	$27.4^{+39.3}_{-15.4}$	
8406	12:36:46.07	62:13:16.9	5.180	27.2	1.7 ± 0.2	$8.37^{+0.19}_{-0.26}$	$-2.23^{+0.08}_{-0.07}$	$0.94^{+0.04}_{-0.09}$	$3.1^{+1.5}_{-1.5}$	[2]
10218	12:37:05.64	62:13:42.1	5.181	26.3	3.4 ± 0.4	$8.96^{+0.37}_{-0.26}$	$-2.21^{+0.06}_{-0.06}$	$0.90^{+0.07}_{-0.17}$	$8.5^{+4.6}_{-2.2}$	
3176	12:36:52.03	62:11:44.9	5.182	25.7	8.7 ± 0.5	$9.20^{+0.41}_{-0.28}$	$-1.56^{+0.14}_{-0.12}$	$0.65^{+0.16}_{-0.13}$	$21.1^{+14.6}_{-11.8}$	
7003	12:36:49.51	62:12:55.2	5.182	26.1	3.9 ± 0.2	$9.44^{+0.32}_{-0.50}$	$-1.88^{+0.14}_{-0.07}$	$0.59^{+0.15}_{-0.20}$	$17.9^{+15.0}_{-5.1}$	
7296	12:36:53.09	62:12:59.5	5.183	26.6	3.6 ± 0.4	$8.65^{+0.34}_{-0.34}$	$-1.89^{+0.08}_{-0.07}$	$0.79^{+0.13}_{-0.12}$	$4.9^{+5.1}_{-2.0}$	[2]
4528	12:36:59.25	62:12:12.3	5.184	26.7	3.7 ± 0.3	$9.34^{+0.29}_{-0.52}$	$-1.16^{+0.16}_{-0.18}$	$0.57^{+0.14}_{-0.14}$	$11.4^{+11.9}_{-10.1}$	
8178	12:36:56.51	62:13:13.5	5.184	26.8	4.3 ± 0.3	$8.75^{+0.20}_{-0.39}$	$-2.21^{+0.10}_{-0.11}$	$0.80^{+0.13}_{-0.32}$	$5.5^{+4.6}_{-3.0}$	[2,4]
4783	12:36:48.71	62:12:16.8	5.185	24.1	38.0 ± 0.7	$10.40^{+0.12}_{-0.25}$	$-0.71^{+0.14}_{-0.09}$	$0.65^{+0.10}_{-0.14}$	$107.0^{+121.0}_{-43.4}$	
HDF850.1	12:36:51.97	62:12:26.0	5.188	24.0	11.0 ± 0.7	$10.4^{+0.3}_{-0.2}$	—	—	—	[1,6]
Extended Structure 4										
1586	12:36:42.60	62:11:04.4	5.177	25.8	3.6 ± 0.4	$9.47^{+0.25}_{-0.39}$	$-1.97^{+0.10}_{-0.08}$	$0.79^{+0.14}_{-0.04}$	$24.5^{+13.9}_{-13.5}$	
128	12:36:36.57	62:09:45.1	5.178	27.5	2.0 ± 0.2	$8.00^{+0.46}_{-0.41}$	$-2.27^{+0.10}_{-0.08}$	$0.93^{+0.04}_{-0.06}$	$1.5^{+1.7}_{-0.6}$	
391	12:36:44.76	62:10:08.8	5.178	—	2.2 ± 0.2	$8.67^{+0.24}_{-0.35}$	$-1.72^{+0.23}_{-0.18}$	$0.65^{+0.14}_{-0.17}$	$4.9^{+4.7}_{-2.8}$	
169	12:36:39.79	62:09:49.1	5.179	25.2	20.0 ± 0.3	$9.93^{+0.18}_{-0.61}$	$-1.60^{+0.14}_{-0.10}$	$0.53^{+0.18}_{-0.17}$	$36.2^{+57.1}_{-17.3}$	[2]
999	12:36:45.47	62:10:46.5	5.181	27.9	4.8 ± 0.2	$7.26^{+0.47}_{-0.12}$	$-2.22^{+0.11}_{-0.10}$	$0.87^{+0.05}_{-0.05}$	$0.4^{+0.5}_{-0.1}$	
1512	12:36:40.72	62:11:02.0	5.182	26.0	5.0 ± 0.4	$8.86^{+0.41}_{-0.26}$	$-2.24^{+0.06}_{-0.06}$	$0.95^{+0.03}_{-0.05}$	$12.2^{+6.1}_{-6.6}$	
1820	12:36:51.79	62:11:11.3	5.182	26.0	12.0 ± 0.3	$9.64^{+0.24}_{-0.28}$	$-1.56^{+0.11}_{-0.10}$	$0.53^{+0.13}_{-0.20}$	$19.6^{+22.3}_{-10.1}$	
1852	12:36:42.17	62:11:12.2	5.184	24.9	7.4 ± 0.6	$10.19^{+0.24}_{-0.48}$	$-1.70^{+0.10}_{-0.10}$	$0.56^{+0.21}_{-0.34}$	$86.9^{+307.9}_{-51.8}$	

 a Typical 1σ spectroscopic redshift uncertainties are ± 0.001 . b 1 = Walter et al. (2012), 2 = Arrabal Haro et al. (2018), 3 = Riechers et al. (2020), 4 = Calvi et al. (2021), 5 = Matthee et al. (2023), 6 = Xiao et al. (2023) c Presented in Xiao et al. (2023)

Table B2. Catalogs of Star-Forming Galaxies at $z \sim 5.15$ -5.32 that are part of the overdensity in the FRESKO GOODS North Field.

ID	RA	DEC	z_{spec}	m_{210} [mag]	$f_{H\alpha}$ [10^{-18} ergs/s/cm 2]	$\log(M_{\star})$	β	A_V	SFR	Ref ^a
Extended Structure 5										
4796	12:36:20.66	62:12:16.8	5.166	26.9	2.7 ± 0.2	$8.85^{+0.18}_{-0.35}$	$-1.85^{+0.19}_{-0.09}$	$0.71^{+0.13}_{-0.25}$	$5.8^{+6.2}_{-3.8}$	
3678	12:36:25.72	62:11:55.1	5.179	27.6	1.8 ± 0.3	$8.33^{+0.25}_{-0.32}$	$-2.12^{+0.16}_{-0.13}$	$0.79^{+0.11}_{-0.17}$	$2.4^{+2.5}_{-1.3}$	
5143	12:36:23.18	62:12:23.3	5.179	27.6	3.5 ± 0.2	$8.15^{+0.33}_{-0.39}$	$-1.49^{+0.23}_{-0.17}$	$0.57^{+0.16}_{-0.10}$	$2.4^{+3.4}_{-1.4}$	
2087	12:36:23.22	62:11:18.3	5.181	26.1	6.1 ± 0.5	$9.32^{+0.59}_{-0.61}$	$-1.76^{+0.14}_{-0.14}$	$0.45^{+0.33}_{-0.26}$	$18.3^{+31.9}_{-10.4}$	
5587	12:36:29.12	62:12:30.7	5.182	27.1	5.2 ± 0.3	$8.62^{+0.26}_{-0.35}$	$-1.84^{+0.21}_{-0.16}$	$0.59^{+0.12}_{-0.21}$	$4.7^{+5.9}_{-2.4}$	
3888	12:36:20.13	62:11:58.6	5.183	25.2	24.0 ± 0.5	$9.72^{+0.30}_{-0.39}$	$-1.40^{+0.12}_{-0.09}$	$0.45^{+0.19}_{-0.12}$	$48.8^{+54.3}_{-20.3}$	
4251	12:36:18.77	62:12:06.3	5.183	27.9	1.5 ± 0.2	$8.45^{+0.20}_{-0.43}$	$-2.04^{+0.16}_{-0.13}$	$0.68^{+0.15}_{-0.13}$	$3.5^{+3.8}_{-1.8}$	
5146	12:36:23.28	62:12:23.0	5.187	26.3	6.7 ± 0.3	$9.30^{+0.20}_{-0.31}$	$-1.40^{+0.15}_{-0.19}$	$0.52^{+0.17}_{-0.14}$	$18.2^{+26.5}_{-10.1}$	
4919	12:36:17.66	62:12:19.3	5.188	27.8	1.7 ± 0.2	$8.46^{+0.26}_{-0.36}$	$-1.95^{+0.16}_{-0.23}$	$0.83^{+0.09}_{-0.13}$	$1.3^{+1.2}_{-0.6}$	
4306	12:36:26.48	62:12:07.4	5.193	26.1	5.1 ± 0.3	$9.55^{+0.20}_{-0.25}$	$-1.67^{+0.11}_{-0.10}$	$0.52^{+0.16}_{-0.25}$	$29.9^{+43.0}_{-17.8}$	[1,2]
Extended Structure 6										
17877	12:37:08.08	62:15:08.2	5.178	28.0	1.9 ± 0.2	$8.56^{+0.48}_{-0.30}$	$-2.02^{+0.12}_{-0.12}$	$0.69^{+0.15}_{-0.41}$	$3.4^{+8.5}_{-2.0}$	
10187	12:37:12.39	62:13:42.1	5.181	27.3	1.5 ± 0.3	$8.31^{+0.38}_{-0.64}$	$-2.13^{+0.12}_{-0.13}$	$0.88^{+0.07}_{-0.13}$	$1.6^{+2.0}_{-0.7}$	
23929	12:37:15.63	62:16:23.5	5.184	25.7	5.6 ± 0.3	$9.59^{+0.24}_{-0.53}$	$-2.15^{+0.08}_{-0.06}$	$0.65^{+0.24}_{-0.35}$	$25.7^{+85.6}_{-9.9}$	[1,2,4]
17512	12:37:12.62	62:15:04.1	5.185	25.4	4.4 ± 0.3	$9.95^{+0.10}_{-0.15}$	$-1.60^{+0.09}_{-0.09}$	$0.72^{+0.14}_{-0.22}$	$17.9^{+30.8}_{-13.6}$	
20673	12:37:17.87	62:15:40.7	5.187	26.7	1.8 ± 0.2	$9.28^{+0.22}_{-0.26}$	$-1.96^{+0.08}_{-0.08}$	$0.50^{+0.22}_{-0.27}$	$16.9^{+34.9}_{-10.7}$	
22471	12:37:15.70	62:16:03.0	5.187	25.1	8.1 ± 0.4	$10.23^{+0.21}_{-0.38}$	$-0.84^{+0.12}_{-0.19}$	$0.52^{+0.14}_{-0.18}$	$35.9^{+62.3}_{-11.9}$	
19988	12:37:14.51	62:15:32.5	5.188	25.3	4.7 ± 0.3	$9.37^{+0.33}_{-0.32}$	$-2.24^{+0.08}_{-0.08}$	$0.94^{+0.04}_{-0.07}$	$26.3^{+17.5}_{-11.3}$	[2,4]
21948	12:37:21.03	62:15:56.6	5.188	28.3	1.0 ± 0.2	$8.04^{+0.18}_{-0.26}$	$-2.15^{+0.08}_{-0.10}$	$0.77^{+0.08}_{-0.17}$	$2.1^{+1.1}_{-0.8}$	
23257	12:37:22.39	62:16:11.3	5.188	26.1	5.1 ± 0.3	$9.25^{+0.18}_{-0.16}$	$-2.03^{+0.09}_{-0.09}$	$0.59^{+0.21}_{-0.20}$	$28.8^{+16.0}_{-14.3}$	
16991	12:37:13.69	62:14:59.1	5.189	26.6	4.5 ± 0.4	$8.76^{+0.32}_{-0.36}$	$-1.89^{+0.08}_{-0.10}$	$0.66^{+0.14}_{-0.14}$	$8.0^{+4.9}_{-3.5}$	
Dusty-7162	12:37:16.90	62:14:00.9	5.189	25.1	30.0 ± 0.6	$>9.8^c$	$—^c$	$—^c$	$—^c$	[6]
17347	12:37:13.70	62:15:02.5	5.189	28.1	2.2 ± 0.3	$8.26^{+0.38}_{-0.43}$	$-1.30^{+0.28}_{-0.27}$	$0.56^{+0.18}_{-0.15}$	$1.9^{+2.3}_{-0.9}$	
20278	12:37:15.33	62:15:35.5	5.189	25.9	6.8 ± 0.3	$9.86^{+0.15}_{-0.17}$	$-1.29^{+0.10}_{-0.13}$	$0.47^{+0.12}_{-0.13}$	$23.0^{+21.8}_{-12.5}$	
21183	12:37:20.93	62:15:47.2	5.189	27.0	2.7 ± 0.3	$8.37^{+0.50}_{-0.34}$	$-2.16^{+0.12}_{-0.10}$	$0.84^{+0.09}_{-0.10}$	$2.9^{+7.0}_{-1.6}$	
23256	12:37:22.28	62:16:13.2	5.191	25.2	5.6 ± 0.5	$9.74^{+0.41}_{-0.45}$	$-1.67^{+0.10}_{-0.12}$	$0.73^{+0.14}_{-0.27}$	$54.7^{+104.4}_{-24.1}$	
16264	12:37:14.53	62:14:51.5	5.192	26.1	8.2 ± 0.4	$9.59^{+0.16}_{-0.16}$	$-1.67^{+0.08}_{-0.10}$	$0.50^{+0.12}_{-0.12}$	$21.7^{+20.5}_{-10.2}$	
22058	12:37:20.97	62:15:58.0	5.192	27.1	4.1 ± 0.2	$8.72^{+0.26}_{-0.31}$	$-2.04^{+0.10}_{-0.09}$	$0.53^{+0.22}_{-0.16}$	$8.7^{+11.6}_{-4.5}$	
22414	12:37:18.99	62:16:02.7	5.193	26.9	3.4 ± 0.3	$8.65^{+0.38}_{-0.36}$	$-2.01^{+0.11}_{-0.09}$	$0.84^{+0.09}_{-0.09}$	$4.0^{+2.3}_{-2.1}$	
24946	12:37:11.11	62:16:38.6	5.193	25.3	15.0 ± 0.4	$9.88^{+0.15}_{-0.34}$	$-1.47^{+0.09}_{-0.09}$	$0.48^{+0.17}_{-0.11}$	$49.3^{+34.8}_{-25.5}$	[1,2]
21405	12:37:15.69	62:15:49.8	5.194	26.2	14.0 ± 0.3	$9.39^{+0.17}_{-0.19}$	$-1.54^{+0.10}_{-0.11}$	$0.35^{+0.13}_{-0.13}$	$34.1^{+27.1}_{-15.4}$	
25788	12:37:16.07	62:16:51.7	5.194	25.3	17.0 ± 0.4	$9.50^{+0.31}_{-0.23}$	$-1.92^{+0.14}_{-0.08}$	$0.46^{+0.09}_{-0.14}$	$71.6^{+51.7}_{-30.7}$	
24574	12:37:13.73	62:16:33.2	5.195	28.1	3.1 ± 0.3	$7.96^{+0.54}_{-0.17}$	$-1.75^{+0.15}_{-0.16}$	$0.74^{+0.07}_{-0.10}$	$1.6^{+3.0}_{-0.9}$	
Extended Structure 7										
23345	12:36:58.43	62:16:15.0	5.192	26.2	3.5 ± 0.3	$8.96^{+0.44}_{-0.26}$	$-2.11^{+0.06}_{-0.07}$	$0.80^{+0.10}_{-0.34}$	$13.1^{+14.7}_{-5.7}$	[2,4]
24252	12:36:57.30	62:16:28.6	5.192	27.2	1.5 ± 0.2	$8.21^{+0.23}_{-0.39}$	$-2.31^{+0.04}_{-0.05}$	$0.97^{+0.01}_{-0.03}$	$3.2^{+2.0}_{-1.6}$	
22502	12:37:05.58	62:16:03.9	5.193	25.5	8.7 ± 0.5	$9.58^{+0.25}_{-0.29}$	$-1.95^{+0.12}_{-0.08}$	$0.51^{+0.17}_{-0.13}$	$44.0^{+43.6}_{-18.3}$	
24125	12:36:57.36	62:16:26.6	5.193	27.6	1.9 ± 0.2	$8.76^{+0.21}_{-0.26}$	$-1.91^{+0.09}_{-0.10}$	$0.68^{+0.14}_{-0.23}$	$2.8^{+4.5}_{-1.4}$	
22858	12:37:06.63	62:16:08.7	5.194	27.2	3.5 ± 0.3	$8.70^{+0.23}_{-0.33}$	$-1.50^{+0.17}_{-0.15}$	$0.64^{+0.09}_{-0.07}$	$5.3^{+4.5}_{-2.7}$	
Dusty-16116	12:36:56.62	62:17:08.0	5.194	28.2	2.9 ± 0.2	$9.09^{+0.20}_{-0.13}$	$-1.88^{+0.09}_{-0.08}$	$0.14^{+0.06}_{-0.04}$	$24.1^{+9.5}_{-7.8}$	[6]
22295	12:37:05.52	62:16:01.3	5.195	27.4	3.6 ± 0.3	$7.73^{+0.64}_{-0.23}$	$-2.33^{+0.15}_{-0.11}$	$0.94^{+0.04}_{-0.05}$	$0.8^{+0.5}_{-0.2}$	[2,4]
22826	12:37:03.90	62:16:08.4	5.195	27.6	1.3 ± 0.2	$8.61^{+0.30}_{-0.30}$	$-2.14^{+0.09}_{-0.08}$	$0.82^{+0.13}_{-0.13}$	$4.9^{+4.3}_{-1.9}$	
16423	12:37:03.28	62:14:53.4	5.200	27.6	3.0 ± 0.2	$8.15^{+0.29}_{-0.32}$	$-1.83^{+0.13}_{-0.14}$	$0.63^{+0.11}_{-0.12}$	$2.5^{+2.1}_{-1.1}$	
Extended Structure 8										
16542	12:36:59.68	62:14:54.4	5.178	25.3	12.0 ± 0.5	$10.01^{+0.11}_{-0.12}$	$-1.02^{+0.11}_{-0.13}$	$0.66^{+0.09}_{-0.14}$	$49.7^{+54.6}_{-31.0}$	
14125	12:36:50.06	62:14:28.7	5.182	27.5	1.5 ± 0.2	$8.48^{+0.17}_{-0.19}$	$-2.04^{+0.09}_{-0.12}$	$0.74^{+0.12}_{-0.14}$	$5.1^{+2.8}_{-2.2}$	
20034	12:36:55.50	62:15:32.8	5.187	26.5	10.0 ± 0.2	$8.27^{+0.52}_{-0.20}$	$-2.06^{+0.06}_{-0.13}$	$0.80^{+0.07}_{-0.08}$	$4.1^{+6.8}_{-1.7}$	[1,2]
19533	12:36:56.35	62:15:27.0	5.188	25.3	13.0 ± 0.3	$9.76^{+0.19}_{-0.31}$	$-1.49^{+0.08}_{-0.11}$	$0.46^{+0.19}_{-0.19}$	$85.4^{+86.1}_{-51.9}$	
21166	12:36:52.21	62:15:47.2	5.188	27.4	1.5 ± 0.2	$8.52^{+0.18}_{-0.19}$	$-2.24^{+0.09}_{-0.09}$	$0.87^{+0.07}_{-0.26}$	$4.5^{+3.5}_{-2.2}$	
22601	12:36:52.34	62:16:05.1	5.189	25.3	8.1 ± 0.5	$9.38^{+0.50}_{-0.26}$	$-1.86^{+0.09}_{-0.10}$	$0.72^{+0.14}_{-0.26}$	$31.4^{+32.7}_{-15.7}$	
20499	12:36:49.23	62:15:38.6	5.190	25.1	18.0 ± 0.4	$9.19^{+0.22}_{-0.27}$	$-2.33^{+0.06}_{-0.05}$	$0.88^{+0.07}_{-0.20}$	$22.1^{+18.8}_{-11.7}$	[1,2]
21309	12:36:55.39	62:15:48.8	5.191	26.8	3.6 ± 0.2	$8.71^{+0.28}_{-0.46}$	$-2.17^{+0.08}_{-0.08}$	$0.60^{+0.23}_{-0.15}$	$9.6^{+7.5}_{-5.6}$	[1,2]

Table B3. Catalogs of Star-Forming Galaxies at $z \sim 5.15$ -5.32 that are part of the overdensity in the FRESCO GOODS North Field.

ID	RA	DEC	z_{spec}	m_{210} [mag]	$f_{H\alpha}$ [10^{-18} ergs/s/cm 2]	$\log(M_{\star})$	β	A_V	SFR	Ref ^a
Extended Structure 9										
26025	12:36:43.38	62:16:56.1	5.186	26.2	8.9 ± 0.3	$9.39^{+0.18}_{-0.20}$	$-1.65^{+0.11}_{-0.12}$	$0.45^{+0.13}_{-0.09}$	$31.4^{+14.8}_{-11.7}$	
24928	12:36:40.75	62:16:38.3	5.188	25.1	7.8 ± 0.4	$9.84^{+0.14}_{-0.12}$	$-1.20^{+0.11}_{-0.10}$	$0.80^{+0.05}_{-0.14}$	$38.5^{+24.1}_{-23.5}$	
24849	12:36:40.71	62:16:37.4	5.190	27.2	2.4 ± 0.2	$8.91^{+0.27}_{-0.41}$	$-1.51^{+0.12}_{-0.16}$	$0.66^{+0.18}_{-0.19}$	$6.1^{+4.9}_{-3.5}$	
26502	12:36:47.26	62:17:04.2	5.191	26.0	2.6 ± 0.2	$9.55^{+0.28}_{-0.27}$	$-2.14^{+0.06}_{-0.07}$	$0.65^{+0.22}_{-0.40}$	$30.5^{+62.4}_{-17.9}$	
28034	12:36:52.80	62:17:36.2	5.196	28.1	0.7 ± 0.1	$8.07^{+0.30}_{-0.19}$	$-2.35^{+0.13}_{-0.08}$	$0.86^{+0.10}_{-0.16}$	$2.4^{+1.7}_{-0.9}$	
Extended Structure 10										
29679	12:36:39.72	62:18:24.8	5.192	25.7	4.4 ± 0.3	$9.58^{+0.28}_{-0.28}$	$-1.99^{+0.07}_{-0.09}$	$0.57^{+0.33}_{-0.34}$	$39.5^{+88.1}_{-26.2}$	
29651	12:36:39.67	62:18:23.8	5.194	27.6	1.1 ± 0.1	$8.32^{+0.23}_{-0.17}$	$-2.11^{+0.14}_{-0.15}$	$0.76^{+0.10}_{-0.17}$	$4.6^{+2.6}_{-1.5}$	
29544	12:36:39.98	62:18:20.2	5.195	25.5	10.0 ± 0.3	$9.97^{+0.38}_{-0.39}$	$-1.24^{+0.12}_{-0.12}$	$0.43^{+0.24}_{-0.17}$	$60.1^{+109.7}_{-35.6}$	
Extended Structure 11										
6921	12:36:59.18	62:12:53.7	5.208	24.9	13.0 ± 0.3	$9.89^{+0.26}_{-0.52}$	$-1.22^{+0.09}_{-0.08}$	$0.54^{+0.26}_{-0.13}$	$60.7^{+66.4}_{-52.5}$	
9370	12:37:03.31	62:13:31.4	5.212	25.7	20.0 ± 0.4	$9.48^{+0.14}_{-0.22}$	$-1.94^{+0.08}_{-0.07}$	$0.42^{+0.10}_{-0.09}$	$57.6^{+32.5}_{-23.8}$	[1,4]
3374	12:37:00.92	62:11:49.3	5.219	26.9	4.9 ± 0.2	$8.80^{+0.30}_{-0.46}$	$-1.17^{+0.20}_{-0.18}$	$0.53^{+0.14}_{-0.12}$	$8.6^{+8.9}_{-4.5}$	
5204	12:37:08.53	62:12:24.5	5.219	25.5	5.7 ± 0.2	$9.87^{+0.35}_{-0.27}$	$-1.89^{+0.11}_{-0.08}$	$0.59^{+0.21}_{-0.47}$	$57.5^{+329.2}_{-36.8}$	
3023	12:37:02.80	62:11:41.7	5.220	—	4.3 ± 0.2	$9.24^{+0.33}_{-0.33}$	$-1.79^{+0.17}_{-0.20}$	$0.58^{+0.18}_{-0.20}$	$18.2^{+19.1}_{-12.1}$	
5396	12:37:01.03	62:12:27.7	5.221	26.6	3.7 ± 0.2	$9.05^{+0.23}_{-0.21}$	$-1.73^{+0.10}_{-0.10}$	$0.56^{+0.18}_{-0.23}$	$17.0^{+13.4}_{-10.6}$	
Dusty-4014	12:37:12.03	62:12:43.4	5.221	—	—	$>9.8^c$	—	—	—	[5,6]
4927	12:36:59.79	62:12:18.7	5.222	23.9	35.0 ± 0.7	$10.42^{+0.19}_{-0.30}$	$-1.69^{+0.16}_{-0.09}$	$0.62^{+0.13}_{-0.15}$	$103.7^{+190.0}_{-64.1}$	
5702	12:37:03.94	62:12:32.9	5.223	25.2	8.2 ± 0.3	$9.95^{+0.12}_{-0.27}$	$-2.01^{+0.06}_{-0.22}$	$0.61^{+0.14}_{-0.22}$	$56.7^{+71.5}_{-9.9}$	
5467	12:37:02.73	62:12:28.8	5.227	25.4	19.0 ± 0.4	$9.68^{+0.15}_{-0.25}$	$-1.55^{+0.09}_{-0.09}$	$0.53^{+0.11}_{-0.15}$	$55.4^{+53.2}_{-16.0}$	[2]
Extended Structure 12										
11160	12:37:18.76	62:13:54.1	5.222	27.9	1.7 ± 0.2	$8.85^{+0.27}_{-0.41}$	$-1.76^{+0.15}_{-0.16}$	$0.71^{+0.15}_{-0.33}$	$4.8^{+8.2}_{-2.7}$	
14954	12:37:21.87	62:14:36.9	5.222	27.4	2.0 ± 0.3	$8.40^{+0.38}_{-0.52}$	$-2.18^{+0.13}_{-0.12}$	$0.92^{+0.05}_{-0.05}$	$2.6^{+1.4}_{-1.1}$	
19541	12:37:26.47	62:15:27.1	5.222	26.5	4.6 ± 0.3	$8.91^{+0.24}_{-0.24}$	$-2.10^{+0.08}_{-0.09}$	$0.62^{+0.16}_{-0.21}$	$14.1^{+9.2}_{-5.2}$	
14421	12:37:20.58	62:14:31.3	5.225	26.6	5.1 ± 0.3	$8.77^{+0.25}_{-0.25}$	$-1.77^{+0.18}_{-0.13}$	$0.60^{+0.16}_{-0.10}$	$9.5^{+6.4}_{-4.9}$	
15403	12:37:21.78	62:14:41.4	5.225	26.9	4.8 ± 0.3	$8.65^{+0.20}_{-0.22}$	$-2.02^{+0.08}_{-0.10}$	$0.60^{+0.15}_{-0.11}$	$8.6^{+4.8}_{-3.3}$	
Extended Structure 13										
26892	12:36:34.87	62:17:11.7	5.259	27.2	1.1 ± 0.2	$8.63^{+0.23}_{-0.27}$	$-2.13^{+0.10}_{-0.10}$	$0.79^{+0.17}_{-0.24}$	$3.9^{+6.0}_{-2.7}$	
21513	12:36:34.97	62:15:51.4	5.267	26.1	3.8 ± 0.2	$9.00^{+0.39}_{-0.24}$	$-1.85^{+0.09}_{-0.08}$	$0.74^{+0.11}_{-0.20}$	$12.6^{+15.2}_{-5.0}$	
26742	12:36:34.19	62:17:08.6	5.267	26.3	9.6 ± 0.3	$8.63^{+0.25}_{-0.42}$	$-2.23^{+0.11}_{-0.10}$	$0.86^{+0.05}_{-0.08}$	$4.6^{+3.4}_{-1.7}$	[2]
26941	12:36:31.44	62:17:12.6	5.269	26.2	4.2 ± 0.3	$9.53^{+0.16}_{-0.91}$	$-1.09^{+0.19}_{-0.11}$	$0.63^{+0.16}_{-0.23}$	$12.7^{+33.1}_{-4.7}$	
27133	12:36:38.35	62:17:16.7	5.277	26.9	2.2 ± 0.3	$8.59^{+0.18}_{-0.24}$	$-2.06^{+0.10}_{-0.12}$	$0.85^{+0.07}_{-0.10}$	$7.4^{+3.6}_{-2.8}$	
Extended Structure 14										
15414	12:36:32.08	62:14:42.0	5.259	27.5	1.7 ± 0.2	$8.72^{+0.30}_{-0.38}$	$-1.80^{+0.17}_{-0.13}$	$0.57^{+0.19}_{-0.17}$	$7.3^{+6.3}_{-4.1}$	
15714	12:36:30.19	62:14:45.1	5.260	27.0	1.9 ± 0.2	$9.13^{+0.15}_{-0.28}$	$-1.76^{+0.17}_{-0.15}$	$0.48^{+0.25}_{-0.20}$	$10.6^{+16.7}_{-7.4}$	
19203	12:36:31.94	62:15:23.6	5.268	27.8	2.7 ± 0.2	$8.21^{+0.23}_{-0.27}$	$-2.22^{+0.08}_{-0.09}$	$0.82^{+0.09}_{-0.11}$	$2.1^{+1.4}_{-1.0}$	
12288	12:36:28.30	62:14:07.9	5.269	27.8	2.0 ± 0.1	$8.24^{+0.14}_{-0.28}$	$-2.30^{+0.11}_{-0.11}$	$0.83^{+0.09}_{-0.22}$	$2.6^{+2.0}_{-1.4}$	
12805	12:36:30.28	62:14:13.8	5.269	26.7	2.7 ± 0.3	$8.64^{+0.33}_{-0.35}$	$-2.09^{+0.07}_{-0.08}$	$0.76^{+0.10}_{-0.17}$	$7.2^{+5.9}_{-4.1}$	
15715	12:36:30.18	62:14:45.4	5.269	27.0	2.1 ± 0.2	$8.59^{+0.19}_{-0.19}$	$-2.08^{+0.11}_{-0.10}$	$0.68^{+0.12}_{-0.21}$	$7.5^{+4.1}_{-2.9}$	
17226	12:36:39.34	62:15:01.6	5.269	27.2	3.0 ± 0.2	$8.07^{+0.32}_{-0.30}$	$-1.99^{+0.09}_{-0.10}$	$0.82^{+0.07}_{-0.10}$	$1.7^{+1.0}_{-0.6}$	
12538	12:36:28.58	62:14:10.5	5.271	25.9	7.6 ± 0.3	$9.33^{+0.21}_{-0.22}$	$-2.18^{+0.08}_{-0.08}$	$0.43^{+0.24}_{-0.15}$	$39.2^{+28.7}_{-19.1}$	
14448	12:36:29.80	62:14:32.0	5.271	26.8	3.8 ± 0.2	$9.04^{+0.18}_{-0.74}$	$-2.01^{+0.10}_{-0.11}$	$0.60^{+0.23}_{-0.25}$	$8.7^{+12.3}_{-5.3}$	
13292	12:36:28.81	62:14:19.2	5.273	26.2	7.7 ± 0.3	$9.12^{+0.23}_{-0.20}$	$-2.05^{+0.08}_{-0.07}$	$0.38^{+0.21}_{-0.13}$	$24.3^{+18.6}_{-10.9}$	
13254	12:36:28.71	62:14:18.8	5.275	25.9	5.3 ± 0.4	$9.28^{+0.19}_{-0.20}$	$-2.08^{+0.07}_{-0.06}$	$0.53^{+0.23}_{-0.14}$	$29.9^{+15.8}_{-12.7}$	
16223	12:36:37.10	62:14:51.1	5.276	26.5	4.2 ± 0.3	$9.41^{+0.24}_{-0.27}$	$-1.83^{+0.10}_{-0.09}$	$0.53^{+0.31}_{-0.21}$	$11.5^{+14.7}_{-7.5}$	
Extended Structure 15										
13539	12:36:22.73	62:14:21.7	5.296	26.4	7.3 ± 0.3	$9.58^{+0.14}_{-0.23}$	$-1.67^{+0.08}_{-0.10}$	$0.37^{+0.22}_{-0.09}$	$26.6^{+26.2}_{-12.5}$	
13540	12:36:22.78	62:14:22.1	5.297	26.1	6.0 ± 0.3	$9.45^{+0.12}_{-0.57}$	$-2.03^{+0.16}_{-0.07}$	$0.75^{+0.12}_{-0.19}$	$14.2^{+18.0}_{-7.0}$	
13668	12:36:28.66	62:14:23.8	5.298	25.4	6.3 ± 0.3	$9.86^{+0.14}_{-0.35}$	$-1.54^{+0.08}_{-0.11}$	$0.58^{+0.22}_{-0.24}$	$63.8^{+86.5}_{-47.7}$	
12799	12:36:20.13	62:14:13.7	5.300	26.9	4.6 ± 0.2	$8.81^{+0.25}_{-0.37}$	$-2.09^{+0.10}_{-0.09}$	$0.68^{+0.11}_{-0.11}$	$5.8^{+6.5}_{-1.6}$	
17951	12:36:31.18	62:15:09.0	5.300	26.2	4.9 ± 0.2	$8.87^{+0.22}_{-0.24}$	$-2.18^{+0.07}_{-0.08}$	$0.73^{+0.13}_{-0.27}$	$13.3^{+9.0}_{-5.9}$	
12566	12:36:32.81	62:14:10.7	5.303	25.4	12.0 ± 0.3	$9.69^{+0.26}_{-0.34}$	$-0.94^{+0.11}_{-0.08}$	$0.67^{+0.10}_{-0.13}$	$29.0^{+30.5}_{-12.5}$	
13750	12:36:24.20	62:14:24.7	5.305	26.8	1.6 ± 0.2	$9.09^{+0.27}_{-0.31}$	$-2.00^{+0.14}_{-0.06}$	$0.76^{+0.15}_{-0.25}$	$7.7^{+8.7}_{-4.1}$	
GN10	12:36:33.42	62:14:08.6	5.306	—	—	$>9.7^c$	—	—	—	[3,6]

Table B4. Catalogs of Star-Forming Galaxies at $z \sim 5.15$ - 5.32 that are part of the overdensity in the FRESCO GOODS North Field.

ID	RA	DEC	z_{spec}	m_{210} [mag]	$f_{H\alpha}$ [10^{-18} ergs/s/cm 2]	$\log(M_{\star})$	β	A_V	SFR	Ref a
Extended Structure 16										
27663	12:36:29.26	62:17:27.6	5.300	26.8	2.2 ± 0.2	$9.24^{+0.30}_{-0.40}$	$-1.67^{+0.13}_{-0.14}$	$0.59^{+0.13}_{-0.26}$	$12.1^{+28.2}_{-7.1}$	
28064	12:36:29.10	62:17:36.9	5.300	29.6	2.2 ± 0.1	$8.01^{+0.45}_{-0.46}$	$-1.80^{+0.21}_{-0.17}$	$0.68^{+0.12}_{-0.16}$	$1.1^{+2.3}_{-0.7}$	
28057	12:36:31.65	62:17:36.8	5.303	27.2	1.4 ± 0.1	$8.42^{+0.15}_{-0.25}$	$-1.82^{+0.10}_{-0.15}$	$0.80^{+0.08}_{-0.18}$	$5.2^{+2.3}_{-2.2}$	
Extended Structure 17										
22442	12:37:19.75	62:16:02.8	5.297	26.4	2.6 ± 0.2	$9.46^{+0.26}_{-0.42}$	$-1.89^{+0.10}_{-0.06}$	$0.58^{+0.22}_{-0.22}$	$22.3^{+14.8}_{-10.2}$	
23444	12:37:19.58	62:16:16.2	5.299	26.7	5.0 ± 0.2	$9.05^{+0.19}_{-0.21}$	$-1.10^{+0.14}_{-0.14}$	$0.54^{+0.11}_{-0.15}$	$19.6^{+11.4}_{-8.2}$	
19151	12:37:18.77	62:15:22.7	5.305	24.5	17.0 ± 0.5	$10.00^{+0.35}_{-0.26}$	$-1.43^{+0.08}_{-0.15}$	$0.69^{+0.08}_{-0.12}$	$100.5^{+100.2}_{-53.4}$	
16469	12:37:20.03	62:14:53.3	5.308	26.2	6.0 ± 0.4	$9.59^{+0.28}_{-0.54}$	$-1.05^{+0.15}_{-0.26}$	$0.66^{+0.14}_{-0.17}$	$11.1^{+12.4}_{-5.5}$	
Extended Structure 18										
315	12:36:39.31	62:10:03.4	5.302	26.0	6.2 ± 0.2	$9.10^{+0.22}_{-0.51}$	$-1.70^{+0.12}_{-0.15}$	$0.66^{+0.12}_{-0.21}$	$20.6^{+13.6}_{-13.6}$	
69	12:36:36.44	62:09:36.8	5.309	27.3	0.8 ± 0.1	$8.64^{+0.16}_{-0.40}$	$-2.20^{+0.12}_{-0.09}$	$0.75^{+0.17}_{-0.33}$	$5.6^{+6.3}_{-1.5}$	
67	12:36:40.27	62:09:36.7	5.313	—	2.6 ± 0.1	$9.09^{+0.16}_{-0.61}$	$-2.01^{+0.16}_{-0.08}$	$0.75^{+0.17}_{-0.49}$	$8.3^{+38.4}_{-4.1}$	
Outside Extended Structures										
13227	12:36:58.22	62:14:18.7	5.151	27.7	1.2 ± 0.2	$8.51^{+0.25}_{-0.30}$	$-1.92^{+0.16}_{-0.15}$	$0.73^{+0.16}_{-0.28}$	$4.7^{+4.9}_{-3.5}$	
2152	12:36:25.39	62:11:19.8	5.161	25.6	15.0 ± 0.3	$9.57^{+0.25}_{-0.49}$	$-1.27^{+0.15}_{-0.11}$	$0.53^{+0.14}_{-0.23}$	$31.5^{+45.1}_{-15.4}$	
2096	12:36:24.97	62:11:18.2	5.163	25.7	5.3 ± 0.4	$9.79^{+0.18}_{-0.27}$	$-1.52^{+0.23}_{-0.20}$	$0.50^{+0.23}_{-0.17}$	$37.5^{+72.0}_{-25.9}$	
23280	12:37:22.17	62:16:14.0	5.165	26.9	4.1 ± 0.3	$8.51^{+0.31}_{-0.41}$	$-1.57^{+0.20}_{-0.27}$	$0.60^{+0.18}_{-0.14}$	$4.9^{+5.6}_{-2.5}$	
19527	12:36:38.42	62:15:27.2	5.189	25.7	5.1 ± 0.4	$9.78^{+0.12}_{-0.07}$	$-1.17^{+0.10}_{-0.15}$	$0.72^{+0.09}_{-0.26}$	$31.0^{+41.6}_{-16.2}$	[2]
29562	12:36:52.33	62:18:20.9	5.191	27.8	1.4 ± 0.2	$8.26^{+0.31}_{-0.23}$	$-2.27^{+0.10}_{-0.07}$	$0.91^{+0.07}_{-0.12}$	$2.0^{+2.5}_{-1.2}$	
8937	12:37:17.34	62:13:25.2	5.191	25.8	7.3 ± 0.3	$9.32^{+0.21}_{-0.44}$	$-2.04^{+0.09}_{-0.07}$	$0.77^{+0.11}_{-0.22}$	$15.1^{+16.3}_{-7.2}$	[2]
8947	12:37:17.16	62:13:25.4	5.196	27.8	1.1 ± 0.1	$8.83^{+0.35}_{-0.26}$	$-1.61^{+0.18}_{-0.17}$	$0.55^{+0.26}_{-0.29}$	$7.2^{+12.0}_{-5.2}$	
10911	12:36:24.08	62:13:51.2	5.197	26.3	3.6 ± 0.3	$9.40^{+0.12}_{-0.38}$	$-1.96^{+0.07}_{-0.04}$	$0.64^{+0.09}_{-0.27}$	$14.1^{+13.5}_{-9.6}$	[2]
9073	12:37:01.85	62:13:27.6	5.202	26.6	2.8 ± 0.4	$9.13^{+0.33}_{-0.39}$	$-1.76^{+0.12}_{-0.13}$	$0.65^{+0.18}_{-0.09}$	$11.0^{+9.8}_{-6.6}$	
74	12:36:40.52	62:09:37.9	5.207	—	2.1 ± 0.2	$8.41^{+0.44}_{-0.49}$	$-2.04^{+0.17}_{-0.15}$	$0.82^{+0.09}_{-0.11}$	$2.5^{+2.9}_{-1.2}$	
23026	12:36:19.92	62:16:10.9	5.208	27.6	2.1 ± 0.2	$8.61^{+0.21}_{-0.38}$	$-2.02^{+0.15}_{-0.11}$	$0.66^{+0.16}_{-0.33}$	$4.6^{+7.6}_{-2.5}$	
16253	12:37:01.00	62:14:51.6	5.209	28.2	1.1 ± 0.2	$7.99^{+0.34}_{-0.49}$	$-1.74^{+0.20}_{-0.18}$	$0.75^{+0.10}_{-0.20}$	$1.4^{+2.1}_{-0.7}$	
10200	12:36:22.49	62:13:42.3	5.216	27.6	6.9 ± 0.2	$7.92^{+0.22}_{-0.19}$	$-2.18^{+0.13}_{-0.14}$	$0.75^{+0.10}_{-0.07}$	$1.6^{+0.8}_{-0.8}$	
28662	12:37:06.58	62:17:53.2	5.216	27.4	1.3 ± 0.2	$8.58^{+0.19}_{-0.49}$	$-2.15^{+0.13}_{-0.10}$	$0.76^{+0.15}_{-0.23}$	$3.8^{+4.0}_{-2.1}$	
6061	12:37:13.38	62:12:39.1	5.220	—	11.0 ± 0.3	$9.51^{+0.10}_{-0.26}$	$-2.14^{+0.09}_{-0.09}$	$0.64^{+0.19}_{-0.22}$	$57.9^{+24.0}_{-27.2}$	[2]
2930	12:36:22.49	62:11:39.5	5.222	23.5	5.0 ± 0.2	$11.07^{+0.13}_{-0.20}$	$-0.84^{+0.12}_{-0.16}$	$0.45^{+0.34}_{-0.15}$	$224.2^{+497.3}_{-187.2}$	
514	12:36:43.77	62:10:18.0	5.223	27.5	2.2 ± 0.2	$8.55^{+0.34}_{-0.32}$	$-1.96^{+0.16}_{-0.16}$	$0.74^{+0.17}_{-0.20}$	$3.7^{+5.2}_{-1.9}$	
8544	12:37:14.58	62:13:18.9	5.223	26.1	4.8 ± 0.2	$9.41^{+0.34}_{-0.21}$	$-1.44^{+0.13}_{-0.11}$	$0.51^{+0.15}_{-0.12}$	$43.3^{+26.2}_{-22.3}$	
21767	12:37:00.98	62:15:54.5	5.224	28.8	1.1 ± 0.1	$7.80^{+0.60}_{-0.70}$	$-1.91^{+0.21}_{-0.29}$	$0.74^{+0.16}_{-0.27}$	$0.4^{+1.6}_{-0.2}$	
24801	12:37:00.32	62:16:36.7	5.224	27.6	1.3 ± 0.2	$8.65^{+0.19}_{-0.37}$	$-2.10^{+0.08}_{-0.11}$	$0.72^{+0.19}_{-0.31}$	$4.7^{+5.6}_{-2.4}$	
11969	12:36:27.57	62:14:05.5	5.227	26.6	2.2 ± 0.3	$8.07^{+0.57}_{-0.24}$	$-2.22^{+0.08}_{-0.09}$	$0.91^{+0.05}_{-0.07}$	$2.5^{+4.0}_{-1.1}$	
22259	12:37:06.39	62:16:00.9	5.227	27.9	2.0 ± 0.3	$8.24^{+0.42}_{-0.33}$	$-2.14^{+0.13}_{-0.12}$	$0.79^{+0.12}_{-0.33}$	$2.5^{+2.7}_{-1.5}$	
17190	12:37:05.38	62:15:01.3	5.234	27.3	1.7 ± 0.2	$8.79^{+0.25}_{-0.45}$	$-2.10^{+0.09}_{-0.09}$	$0.84^{+0.10}_{-0.47}$	$4.1^{+6.6}_{-1.4}$	
19141	12:37:06.47	62:15:22.8	5.234	25.6	4.9 ± 0.4	$9.21^{+0.25}_{-0.18}$	$-2.26^{+0.08}_{-0.06}$	$0.82^{+0.13}_{-0.25}$	$24.6^{+29.6}_{-8.7}$	
21117	12:37:22.14	62:15:46.2	5.238	25.3	5.8 ± 0.5	$9.84^{+0.18}_{-0.26}$	$-1.73^{+0.14}_{-0.08}$	$0.64^{+0.15}_{-0.32}$	$61.2^{+113.4}_{-44.9}$	
21282	12:37:22.63	62:15:48.1	5.240	26.9	12.0 ± 0.3	$10.82^{+0.11}_{-0.31}$	$-1.49^{+0.09}_{-0.04}$	$0.01^{+0.01}_{-0.00}$	$841.2^{+528.9}_{-322.7}$	
7135	12:36:19.66	62:12:56.8	5.246	27.5	9.9 ± 0.3	$7.57^{+0.15}_{-0.11}$	$-1.99^{+0.12}_{-0.13}$	$0.78^{+0.08}_{-0.08}$	$0.7^{+0.3}_{-0.1}$	
21068	12:36:11.21	62:15:45.8	5.247	28.1	1.4 ± 0.1	$8.41^{+0.31}_{-0.53}$	$-2.06^{+0.12}_{-0.11}$	$0.73^{+0.13}_{-0.18}$	$2.5^{+2.4}_{-1.5}$	
12053	12:36:22.48	62:14:05.3	5.248	27.4	2.2 ± 0.2	$8.37^{+0.38}_{-0.32}$	$-1.88^{+0.11}_{-0.12}$	$0.61^{+0.18}_{-0.15}$	$3.9^{+3.3}_{-2.0}$	
13670	12:37:27.33	62:14:23.6	5.250	26.8	2.0 ± 0.2	$8.37^{+0.40}_{-0.30}$	$-2.28^{+0.08}_{-0.07}$	$0.93^{+0.04}_{-0.14}$	$4.4^{+4.5}_{-2.2}$	
20423	12:37:07.73	62:15:37.4	5.272	25.7	6.5 ± 0.6	$9.56^{+0.29}_{-0.44}$	$-1.22^{+0.09}_{-0.11}$	$0.69^{+0.12}_{-0.23}$	$38.1^{+28.3}_{-22.6}$	
17577	12:37:08.47	62:15:05.0	5.277	26.8	4.5 ± 0.2	$8.39^{+0.34}_{-0.38}$	$-2.28^{+0.08}_{-0.07}$	$0.89^{+0.05}_{-0.04}$	$3.2^{+2.4}_{-1.4}$	
1253	12:36:33.70	62:10:53.7	5.278	25.7	13.0 ± 0.4	$8.95^{+0.34}_{-0.34}$	$-2.18^{+0.10}_{-0.10}$	$0.72^{+0.14}_{-0.10}$	$10.8^{+8.8}_{-7.6}$	
983	12:36:46.13	62:10:44.8	5.280	29.0	1.9 ± 0.2	$6.90^{+0.16}_{-0.10}$	$-2.43^{+0.08}_{-0.05}$	$0.96^{+0.03}_{-0.04}$	$0.1^{+0.1}_{-0.0}$	
12210	12:36:56.60	62:14:07.1	5.284	27.2	2.9 ± 0.2	$7.65^{+1.00}_{-0.39}$	$-2.43^{+0.13}_{-0.09}$	$0.95^{+0.04}_{-0.05}$	$0.4^{+0.3}_{-0.1}$	
29634	12:36:39.58	62:18:23.1	5.288	27.3	1.8 ± 0.2	$8.22^{+0.19}_{-0.22}$	$-1.94^{+0.09}_{-0.10}$	$0.81^{+0.06}_{-0.09}$	$3.4^{+1.4}_{-1.1}$	
7294	12:37:13.04	62:12:59.5	5.292	27.9	10.0 ± 0.2	$7.72^{+0.26}_{-0.21}$	$-1.48^{+0.12}_{-0.12}$	$0.60^{+0.15}_{-0.13}$	$1.0^{+0.8}_{-0.3}$	
8583	12:36:54.23	62:13:19.6	5.295	26.6	2.2 ± 0.2	$9.21^{+0.26}_{-0.50}$	$-2.06^{+0.06}_{-0.08}$	$0.68^{+0.15}_{-0.43}$	$12.1^{+24.2}_{-5.0}$	

Table B5. Catalogs of Star-Forming Galaxies at $z \sim 5.15$ -5.32 that are part of the overdensity in the FRESCO GOODS North Field.

ID	RA	DEC	z_{spec}	m_{210} [mag]	$f_{H\alpha}$ [10^{-18} ergs/s/cm 2]	$\log(M_{\star})$	β	A_V	SFR	Ref ^a
Outside Extended Structures										
11214	12:36:35.85	62:13:54.7	5.296	26.0	7.2 ± 0.2	$9.41^{+0.21}_{-0.25}$	$-1.78^{+0.09}_{-0.09}$	$0.63^{+0.14}_{-0.11}$	$14.7^{+11.7}_{-4.7}$	
2243	12:36:52.12	62:11:22.7	5.296	28.0	2.4 ± 0.3	$8.18^{+0.43}_{-0.30}$	$-2.29^{+0.10}_{-0.15}$	$0.93^{+0.05}_{-0.13}$	$2.0^{+1.6}_{-0.6}$	
10647	12:36:12.62	62:13:47.6	5.297	26.4	2.4 ± 0.1	$9.34^{+0.29}_{-0.30}$	$-1.78^{+0.11}_{-0.12}$	$0.49^{+0.31}_{-0.20}$	$23.4^{+25.8}_{-13.0}$	
6255	12:36:54.32	62:12:42.9	5.307	25.7	6.0 ± 0.4	$9.77^{+0.16}_{-0.16}$	$-1.49^{+0.11}_{-0.07}$	$0.61^{+0.18}_{-0.23}$	$31.5^{+42.2}_{-17.1}$	
17397	12:37:24.83	62:15:02.7	5.310	24.7	42.0 ± 0.6	$9.82^{+0.20}_{-0.18}$	$-1.35^{+0.10}_{-0.11}$	$0.44^{+0.11}_{-0.09}$	$113.8^{+60.3}_{-35.8}$	
15255	12:36:03.80	62:14:39.7	5.315	26.0	3.8 ± 0.3	$9.15^{+0.37}_{-0.28}$	$-2.19^{+0.07}_{-0.10}$	$0.87^{+0.10}_{-0.21}$	$13.2^{+27.5}_{-6.7}$	
24012	12:36:29.52	62:16:25.0	5.316	27.6	1.5 ± 0.2	$8.33^{+0.32}_{-0.53}$	$-1.92^{+0.14}_{-0.14}$	$0.76^{+0.12}_{-0.19}$	$1.7^{+1.9}_{-0.8}$	